Galaxy merger morphologies and time-scales from simulations of equal-mass gas-rich disc mergers

Jennifer M. Lotz,[1][*][†] Patrik Jonsson,[2] T. J. Cox[3][‡] and Joel R. Primack[2]

[1]*National Optical Astronomical Observatory, 950 North Cherry Avenue, Tucson, AZ 85719, USA*
[2]*Department of Physics, University of California, Santa Cruz, CA 95064, USA*
[3]*Harvard–Smithsonian Center for Astrophysics, 60 Garden Street, Cambridge, MA 02138, USA*

ABSTRACT

A key obstacle to understanding the galaxy merger rate and its role in galaxy evolution is the difficulty in constraining the merger properties and time-scales from instantaneous snapshots of the real Universe. The most common way to identify galaxy mergers is by morphology, yet current theoretical calculations of the time-scales for galaxy disturbances are quite crude. We present a morphological analysis of a large suite of GADGET N-body/hydrodynamical equal-mass gas-rich disc galaxy mergers which have been processed through the Monte Carlo radiative transfer code SUNRISE. With the resulting images, we examine the dependence of quantitative morphology (G, M_{20}, C, A) in the SDSS g band on merger stage, dust, viewing angle, orbital parameters, gas properties, supernova feedback and total mass. We find that mergers appear most disturbed in $G - M_{20}$ and asymmetry at the first pass and at the final coalescence of their nuclei, but can have normal quantitative morphologies at other merger stages. The merger observability time-scales depend on the method used to identify the merger as well as the gas fraction, pericentric distance and relative orientation of the merging galaxies. Enhanced star formation peaks after and lasts significantly longer than strong morphological disturbances. Despite their massive bulges, the majority of merger remnants appear disc-like and dusty in g-band light because of the presence of a low-mass star-forming disc.

Key words: galaxies: evolution – galaxies: interactions – galaxies: structure.

1 INTRODUCTION

It remains unknown to what degree present-day galaxies are assembled discretely via the merger of pre-existing galaxies (e.g. Kauffmann, White & Guiderdoni 1993; Somerville, Primack & Faber 2001) or through more continuous processes such as cold gas and dark matter accretion (e.g. Kereš et al. 2005; Dekel & Birnboim 2006). The most obvious way to constrain the importance of galaxy mergers is to count the number of ongoing merger events. However, current observational constraints on the galaxy merger rate are highly uncertain and strongly debated (Kartaltepe et al. 2007; Renzini 2007; Lin et al. 2008; Lotz et al. 2008; Masjedi, Hogg & Blanton 2008; Ryan et al. 2008). Moreover, theoretical predictions for the galaxy merger rate and mass assembly can vary by factors of 10 (Jogee et al. 2008). These discrepancies are partially the result of the non-trivial conversion of the observed number density of galaxy mergers into a galaxy merger rate and the comparison of this galaxy merger rate to the cosmological predictions for dark matter halo assembly (e.g. Berrier et al. 2006; Guo & White 2008; Kitzbichler & White 2008).

Since the realization that the merger of two disc galaxies could produce a spheroidal galaxy (Toomre 1977), spheroidal galaxies, red galaxies and post-starburst galaxies have been used to indirectly trace the role of galaxy mergers in galaxy evolution (e.g. Bell et al. 2004; Hogg et al. 2006; Abraham et al. 2007; Brown et al. 2007; Faber et al. 2007; Hopkins et al. 2007). However, there are multiple ways to quench star formation and produce post-starbursts or red spheroidal galaxies (e.g. Moore, Lake & Katz 1998; Dekel & Birnboim 2006). Also, simulations of galaxy mergers often show significant star formation and disc components well after the merger event (Springel & Hernquist 2005; Cox et al. 2006; Naab, Jesseit & Burkert 2006a; Robertson et al. 2006a; Cox et al. 2008; Khalatyan et al. 2008), thus the photometric and morphological signatures of merger remnants are ambiguous. A merger remnant's star formation history, morphology and kinematics are likely to depend on the properties of the progenitors and the merger conditions, which are increasingly difficult to determine as time passes. Therefore *direct* observations of ongoing galaxy mergers are needed to constrain the role of mergers in galaxy assembly.

[*]E-mail: lotz@noao.edu
[†]NOAO Leo Goldberg Fellow.
[‡]W. M. Keck Fellow.

Galaxy merging is a process that lasts several billion years rather than a short-lived event. The signatures of a galaxy merger change with merger stage, making the identification of galaxy mergers challenging. If hierarchical models of galaxy assembly are correct, then the majority of massive galaxies could be considered an ongoing merger or a merger remnant which will undergo another merger event within a few Gyr (Stewart et al. 2008). We shall define a galaxy merger as a pair of galaxies which are gravitationally bound and whose orbits will dynamically decay such that their nuclei will merge within x billion years, where x is typically 1–3 Gyr for 'major' mergers with mass ratios greater than 1:3.

There are two general approaches to identifying such systems observationally. The first approach is to find close pairs of galaxies before their nuclei have coalesced, either by selecting galaxies close in projected angular separation and line-of-sight radial velocity (e.g. Barton, Geller & Kenyon 2000; Patton et al. 2000; Lin et al. 2004; de Propris et al. 2005; Lin et al. 2008) or by measuring the deprojected correlation function on small scales (Bell et al. 2006a; Masjedi et al. 2006, 2008; Li et al. 2008). The second approach is to identify morphologically disturbed galaxies, some of which will be post-mergers and some of which will be interacting pairs. Morphological disturbances can be found qualitatively through visual inspection (e.g. Bundy, Ellis & Conselice 2005; Brinchmann et al. 1998; Kampczyk et al. 2007), or by quantitative measures such as the Gini coefficient, second-order moment of the brightest 20 per cent of the light (M_{20}), and asymmetry (Abraham et al. 1994; Abraham, van den Bergh & Nair 2003; Conselice 2003; Lotz, Primack & Madau 2004, hereafter LPM04; Scarlata et al. 2007). At present, all quantitative merger indicators are calibrated empirically using galaxies with 'normal' and 'disturbed' visual classifications.

Translating the number of observed merger candidates into a merger rate requires the assumption of an observability time-scale – the time during which one would have identified the system as merging. Until now, this time-scale has been poorly constrained. Close pair studies often assume a dynamical friction time-scale (which varies from 200 Myr to 1 Gyr). However, this value does not take into account the range of possible orbits for the merging system nor the time during which the system would not meet the pair criteria at very large and very small separations. Also, recent comparison of N-body simulations to analytical calculations indicate that analytically derived dynamical friction time-scales can deviate substantially from those predicted by N-body simulations (Boylan-Kolchin, Ma & Quataert 2008; Jiang et al. 2008). Very similar time-scales are also generally assumed for mergers selected using both visual and quantitative morphologies. This assumption is even less likely to be valid given that different morphological selection criteria are sensitive to different stages of the merger process. For example, visual classification using a combination of signatures (e.g. tidal tails, multiple nuclei, shells) is likely to be sensitive for longer time-scales and lower mass merger ratios than current quantitative methods.

The observability time-scale for a particular merger may depend on (1) the method used to identify the merger; (2) the merger parameters (mass ratio, gas properties, bulge/disc ratio, orbits, dust content) and (3) the observational selection (observed wavelength, viewing angle, spatial resolution). Cosmological-scale numerical simulations currently do not have the spatial resolution to directly determine the cosmologically averaged observability time-scale for each method. Therefore, one is required to use a suite of galaxy-scale numerical simulations which span a large range of input merger parameters to constrain the observability time-scales for the different input parameters. Given a sufficiently broad range of merger param-

eters, the observability time-scales for each parameter set may then be weighted by the probability distribution of the mass ratios, gas fraction, etc. which can be computed from current cosmological-scale simulations. An additional complication is that galaxy-scale numerical simulations typically track the distribution of 'particles' (star, gas and dark matter), as opposed to the projected light distribution at a particular wavelength (which is what is observed). A few works have attempted to quantify the observability time-scales using only the stellar particles (Bell et al. 2006b; Conselice 2006) or gas particles (Iono, Yun & Mihos 2004) and ignoring the effects of dust and age-dependent stellar luminosities. While this may be acceptable for gas-poor dissipationless mergers (e.g. Bell et al. 2006b), the appearance of most gas-rich mergers is almost certainly affected strongly by both young stars and dust.

In this paper, we present a first attempt to constrain the observability time-scales for a variety of methods for identifying galaxy mergers. We present a morphological analysis of a large suite of GADGET N-body/SPH equal-mass gas-rich disc galaxy merger simulations which have been processed through the Monte Carlo radiative transfer code SUNRISE. With the resulting images, we examine the dependence of quantitative morphology in the Sloan Digital Sky Survey (SDSS) g band ($\lambda_c = 4686$ Å) on merger stage, dust, viewing angle, orbital parameters, gas properties, supernova feedback and total mass. We constrain the time-scales of quantitative morphology disturbances in Gini coefficient, M_{20}, and asymmetry, and the time-scales during which close pairs lie at projected separations $R_{proj} < 20, 30, 50$ and $100\,h^{-1}$ kpc, assuming $h = 0.7$. Finally, we compare the simulated merger remnant morphologies and star formation rates. In Section 2, we describe the galaxy merger simulations, including the GADGET N-body/SPH calculations, the SUNRISE Monte Carlo radiative transfer calculations, the initial galaxy models and the range of merger parameters explored. In Section 3, we define the morphological quantities G, M_{20}, C and A. We also describe the different observational criteria used to identify galaxy mergers, and define the merger observability time-scale for each method. In Section 4, we present the results of our analysis, and in Section 5 we discuss the implications of these results for finding galaxy mergers, calculating the merger rate, and the properties of merger remnants. A subsequent paper with a similar analysis of unequal-mass mergers is in preparation.

2 GALAXY MERGER SIMULATIONS

2.1 GADGET N-body/SPH simulations

All of the simulations presented in this paper were performed using the N-body/SPH code GADGET (Springel, Yoshida & White 2001). The details of these simulations, their global star formation histories and their remnant properties are discussed in Cox et al. (2004, 2006, 2008). Each galaxy is initially modelled as a disc of stars and gas, a stellar bulge and a dark matter halo. The stellar and dark matter particles are collisionless and are subject to only gravitational forces. The gas particles are also subject to hydrodynamical forces. The baryonic and dark matter particles have gravitational softening lengths of 100 and 400 pc, respectively. The SPH smoothing length for the gas particles indicates the size of the region over which the particle's hydrodynamic quantities are averaged and is required to be greater than half the gravitational softening length or >50 pc. While we use the first version of GADGET (Springel et al. 2001), the smoothed particle hydrodynamics are upgraded to use the 'conservative entropy' version that is described in Springel & Hernquist (2002). The radiative cooling rate $\Lambda_{net}(\rho, u)$ is computed

for a primordial plasma as described in Katz, Weinberg & Hernquist (1996).

Gas particles are transformed into collisionless star particles assuming the Kennicutt–Schmidt law (Kennicutt 1998) where the star formation rate depends on the local gas density $\rho_{\rm gas}$. This occurs in a stochastic sense (Springel & Hernquist 2003) in which each gas particle can spawn one or two new star particles with a probability determined by the star formation rate. These new star particles have typical masses $\sim 10^5\,{\rm M}_\odot$, and are assigned ages based on their formation time and metallicities based on the metallicity of the gas particle from which they are spawned. We adopt the instantaneous recycling approximation for metal production whereby massive stars are assumed to instantly become supernovae, and the metals produced are put back into the gas phase of the particle. In this version of GADGET, metals do not mix and remain in the gas particle in which they are formed. The enriched gas contribution from stellar winds and Type Ia supernovae are ignored. Unlike the metals, there is no recycling of hydrogen and helium to the gas.

Feedback from supernovae is required to produce stable star-forming discs. Energy from supernovae heats and pressurizes the interstellar gas and stabilizes it against gravitational collapse. Because of the limited resolution of most N-body/SPH simulations, the physical processes associated with supernova feedback cannot be directly modelled and must be included using simple prescriptions. We test two supernova feedback models, which are discussed in detail in Cox et al. (2006). Both models assume the supernova feedback energy is dissipated on an 8-Myr time-scale, and have a equation of state parametrized by n, where $P \sim \rho_{\rm gas}^{1+(n/2)}$. The $n = 2$ model treats star-forming gas with a stiff equation of state where the pressure in star-forming regions scales as $P \sim \rho_{\rm gas}^2$, while the $n = 0$ model assumes that this gas is isothermal with an effective temperature $\sim 10^5\,{\rm K}$ ($P \sim \rho_{\rm gas}$). Both feedback models produce stable isolated star-forming discs and predict similar gas consumption during the merger, but the strength and timing of the merger-induced starbursts depend on the feedback model assumed (Cox et al. 2006). No active galactic nuclei (AGN) are included in these simulations. Such AGN are expected to influence the star formation and morphologies only during the post-merger stages (see Section 5 for discussion).

2.2 SUNRISE Monte Carlo radiative transfer processing

SUNRISE is a parallel code which performs full Monte Carlo radiative transfer calculations using an adaptive-mesh refinement grid (Jonsson 2006; Jonsson et al. 2006). This code was developed to calculate the effects of dust on the emission from the GADGET N-body/SPH simulations. SUNRISE can model arbitrary geometries of emitting and absorbing/scattering material with a large spatial dynamical range and efficiently generate images of the emerging radiation viewed from arbitrary points in space. We use SUNRISE v2 for these simulations (Jonsson 2006). Given a particular simulation geometry and viewing angle, SUNRISE v2 performs the Monte Carlo radiative transfer calculation for 20 wavelengths from the far-ultraviolet (FUV) to the mid-infrared and interpolates a resulting spectral energy distribution of 510 wavelengths including the effects of absorption and scattering.

At least 30 time-steps are analysed for each merger simulation. For each GADGET simulation time-step, SUNRISE assigns a spectral energy distribution to each star particle using the STARBURST99 population synthesis models (Leitherer et al. 1999). New star particles are treated as single stellar populations with ages based on their formation time. Bulge star particles form in an instantaneous burst

well before the start of the simulation (8–13 Gyr depending on the galaxy model; see Rocha et al. 2008). Initial disc star particles are assumed to have formed with an exponentially declining star formation starting at the time of the formation of the bulge. The metallicities of the gas and stars of the initial galaxy models decline exponentially with the radius of the disc. The density of dust is linearly proportional to the density of metals in the gas.

The dust attenuation in the initial galaxy models have been found to reproduce the observed galaxy inclination–attenuation relations and the global infrared-to-ultraviolet flux ratios for spiral galaxies (Rocha et al. 2008). During the merger, the gas discs of the initial galaxies become disrupted, resulting in complicated dust geometries. The full radiative transfer calculations done by the SUNRISE v2 code are well suited to determining the effects of complicated dust geometries. However, the dust approximation is limited by the low spatial resolution of the regions of cold gas and star formation in the input GADGET simulations ($\sim 100\,{\rm pc}$). Therefore the attenuation of very young stars may be underestimated, and the effects of clumpy dust and gas on small scales are not included. A future version of SUNRISE will include improved treatment of small scales. The attenuation and infrared luminosities of the output SUNRISE images during the merger have been compared to the available literature for local dusty mergers. Jonsson et al. (2006) found that these simulations reproduce the observed relationships between ultraviolet spectral slope β and the global infrared-to-ultraviolet flux ratio, thus the simulated dust distribution is a reasonable approximation of the dust found in local dusty mergers.

Images in multiple bandpasses (*GALEX* FUV/NUV, SDSS *ugriz*, 2MASS *JHK*) for 11 isotropically positioned viewpoints ('cameras') are generated and the total absorbed bolometric luminosity over all wavelengths/viewing angles is calculated. These cameras are positioned with respect to the plane of the merger orbit at ϕ, θ ($^\circ$) = (0, 0), (0, 79), (72, 79), (144, 79), (216, 79), (288, 79), (0, 127), (72, 127), (144, 127), (216, 127) and (288, 127). In Figs 1 and 2, we show examples of composite SDSS $u - r - z$ images for one of our simulations viewed face-on (camera 0) and edge-on (camera 4). The predicted dust attenuation for the initial undisturbed galaxy models agrees well with observations of dust attenuation in local disc galaxies (Rocha et al. 2008).

2.3 Initial galaxy models

The goal of this paper is to calibrate the morphological disturbance time-scales for merging and interacting galaxies using realistic 'observations' of galaxy merger simulations including the effects of star formation and dust. Dust and star formation have a much stronger effect on gas-rich merger morphologies than dissipationless mergers, hence we examine the mergers of gas-rich disc galaxies. All of the disc galaxy models explored here have relatively small bulge components with stellar bulge-to-disc mass ratios ≤ 0.25. Such low bulge-to-disc ratio galaxies are more likely to experience strong starbursts (Mihos & Hernquist 1996; Cox et al. 2008) and stronger morphological disturbances (Conselice 2006). These galaxies may also be more representative of high-redshift mergers, as bulge-dominated systems are increasingly rare at $z > 1$ (e.g. Ravindranath et al. 2006; Lotz et al. 2008). The structure of dissipationless spheroidal galaxy merger remnants have been studied by several other authors (e.g. Boylan-Kolchin, Ma & Quataert 2005; Naab, Khochfar & Burkert 2006b).

We adopt two general models for gas-rich discs: the 'Sbc' model tuned to match a large, gas-rich Sbc disc galaxy and the 'G-series' of discs with varying mass (G3, G3, G1, G0) with lower gas
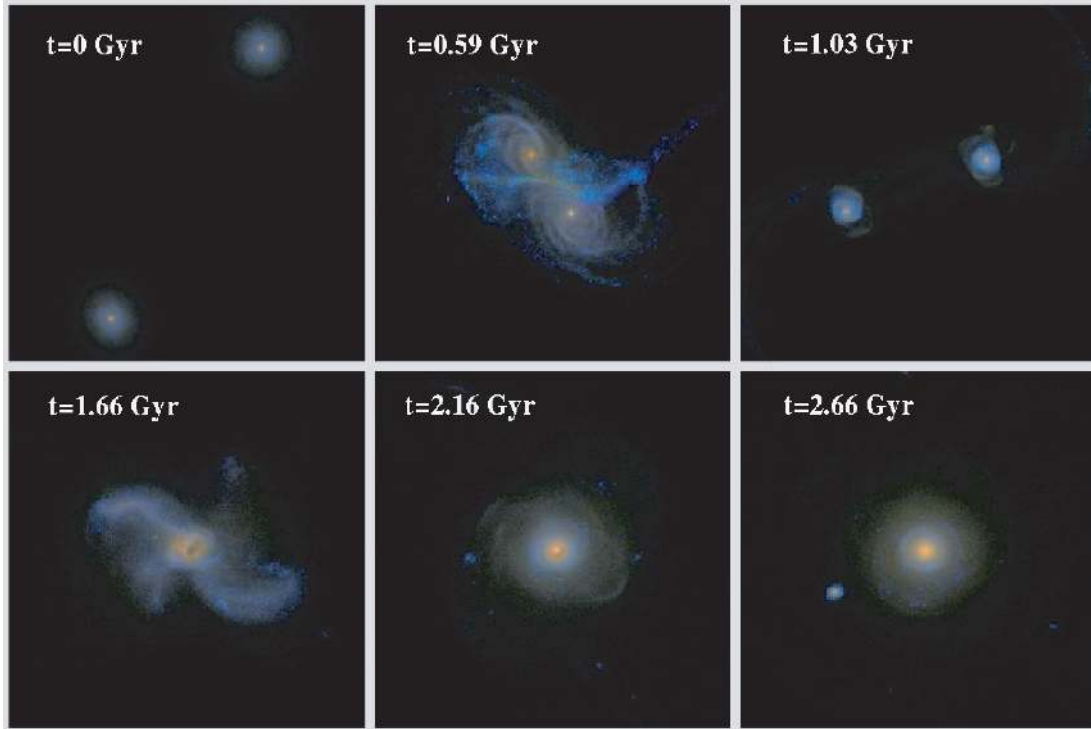
Figure 1. SDSS $u - r - z$ composite colour images with dust extinction for the high-resolution Sbc prograde–prograde simulation (SbcPP×10) as viewed by camera 0 (face-on). Time since the start of the simulation is given in the upper left-hand corner of each image. Shown in the top row are the initial pre-merger galaxies, the first pass, the maximal separation after the first pass, and in the bottom row are the merger of the nuclei, the post-merger at 0.5 Gyr after the merger, and the remnant at 1 Gyr after the merger. The field of view for the initial galaxies and the maximal separation is 200 kpc, while the field of view for the other images is 100 kpc. The merger morphologies are most disturbed at the first pass and merger. Star-forming regions in the initial discs, tidal tails and outer regions of the remnant appear blue, while the dust-enshrouded star-forming nuclei appear red.
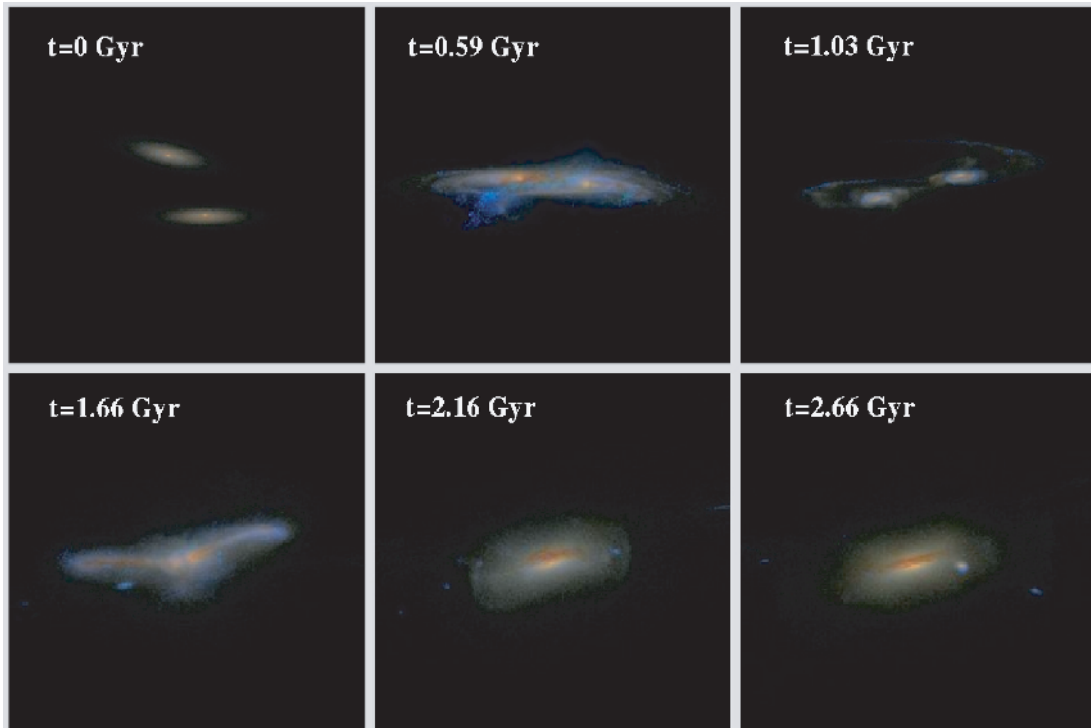
Figure 2. SDSS $u - r - z$ composite colour images for the same simulation as Fig. 1 (SbcPP×10) as viewed by camera 4 (roughly edge-on). Time since the start of the simulation is given in the upper left-hand corner of each image. The time-steps and image scales are same as the previous figure. When viewed edge-on, the dust lanes associated with initial discs and remnants are clearly visible.

Table 1. Initial galaxy conditions.

Model	N_{part}[a]	M_{vir}[b] (M$_\odot$)	C[c]	M_{bary}[d] (M$_\odot$)	M_{disc}^{*}[e] (M$_\odot$)	M_{bulge}^{*}[f] (M$_\odot$)	M_{gas}[g] (M$_\odot$)	f_{bulge}[h]	f_{gas}[i]	R_{disc}[j] (kpc)	R_{bulge}[k] (kpc)	R_{gas}[l] (kpc)
Sbc	1.7×10^5	8.1×10^{11}	11	1.0×10^{11}	3.9×10^{10}	9.7×10^9	5.3×10^{10}	0.10	0.52	5.50	0.45	16.50
G3	2.4×10^5	1.2×10^{12}	6	6.2×10^{10}	4.1×10^{10}	8.9×10^9	1.2×10^{10}	0.14	0.19	2.85	0.62	8.55
G2	1.5×10^5	5.1×10^{11}	9	2.0×10^{10}	1.4×10^{10}	1.5×10^9	4.8×10^9	0.08	0.24	1.91	0.43	5.73
G1	9.5×10^4	2.0×10^{11}	12	7.0×10^9	4.7×10^9	3.0×10^8	2.0×10^9	0.04	0.29	1.48	0.33	4.44
G0	5.1×10^4	5.1×10^{10}	14	1.6×10^9	9.8×10^8	2.0×10^7	6.0×10^8	0.01	0.38	1.12	0.25	3.36

[a]Total number of particles in GADGET simulation for fiducial resolution models. [b]Virial mass. [c]Dark matter halo concentration. [d]Baryonic mass. [e]Mass of stellar disc. [f]Mass of stellar bulge. [g]Mass of gaseous disc. [h]Fraction of baryons in the bulge. [i]Fraction of baryons in gas. [j]Scalelength of stellar disc. [k]Scalelength of bulge. [l]Scalelength of gaseous disc.

fractions tuned to match SDSS observations of local galaxies. (We use the notation of 'Sbc' and 'G' for these different galaxy models in keeping with previous publications based on these simulations: Cox et al. 2006; Jonsson et al. 2006; Cox et al. 2008; Rocha et al. 2008.) Each galaxy model contains a rotationally supported disc of gas and stars, a non-rotating stellar bulge, and a massive dark matter halo (Table 1). A detailed description of the galaxy disc models can be found in Cox et al. (2006, 2008), Jonsson et al. (2006) and Rocha et al. (2008).

The Sbc model parameters are motivated by observations of local gas-rich, disc-dominated Sbc galaxies similar to the Milky Way (see Table 1; Cox et al. 2006). The optical (stellar) disc scalelength, dynamical mass and gas fraction are taken from Roberts & Haynes (1994). The bulge-to-disc ratio and bulge size are from the observations of de Jong (1996) and the total stellar mass is derived using the Bell & de Jong (2001) relations. We assume that the gas disc is exponential with a scalelength three times the stellar disc scalelength (Broeils & van Woerden 1994). We adopt an adiabatically contracted NFW dark matter halo with a concentration of 11. The resulting Sbc model has a viral mass of 8.12×10^{11} M$_\odot$, with a 12.5 per cent baryonic mass fraction. 52 per cent of the baryons are in gas (mostly at large radii), and ~10 per cent of the baryons are bulge stars.

In order to sample the parameter space spanned by many present-day galaxies, we also explored mergers between model galaxies with masses, bulge-to-disc ratios, and gas fractions motivated by SDSS estimates of typical local galaxies (Table 1; Cox et al. 2008). We refer to these model galaxies as the G-series. The largest galaxy (G3) is chosen to have a stellar mass ~5 × 10^{10} M$_\odot$, and the smaller galaxies are chosen to have stellar masses ~1.5 × 10^{10} M$_\odot$ (G2), 0.5 × 10^{10} M$_\odot$ (G1) and 0.1 × 10^{10} M$_\odot$ (G0), spanning a factor of 50 in stellar mass. The stellar half-light radii are from the stellar mass–size relation of Shen et al. (2003). The bulge-to-disc ratios are taken from de Jong (1996) and used to determine the stellar disc and bulge masses and scalelengths. The gas fractions and masses are determined from the gas mass–stellar mass scaling relation from Bell et al. (2003). As for the Sbc model, the gas scalelength is assumed to be three times the stellar disc scalelength. We adopt NFW dark matter halo profiles selected such that the rotation curves lie on the baryonic Tully–Fisher relation (Bell & de Jong 2001; Bell et al. 2003). Unlike the Sbc model, these models do not include adiabatic contraction. The total mass-to-light ratio is assumed to vary with mass such that lower mass galaxy model have higher mass-to-light ratios and the range in total mass is a factor of 23. While the total masses of the Sbc and G3 models are similar, the G3 model has a lower gas fraction, a smaller disc scalelength, and consequently, much less gas at large radii than the Sbc model (Table 1).

Table 2. Equal-mass merger simulation parameters.

Simulation	x[a]	n[b]	θ_1[c]	ϕ_1[c]	θ_2[d]	ϕ_2[d]	e[e]	R_{peri}[f] (kpc)
			Sbc–Sbc mergers					
SbcPP×10	10	2	0	0	30	60	1.00	11
SbcPP×4	4	2	0	0	30	60	1.00	11
SbcPP	1	2	0	0	30	60	1.00	11
SbcPR	1	2	180	0	30	60	1.00	11
SbcRR	1	2	180	0	210	60	1.00	11
SbcPPr−	1	2	0	0	30	60	1.00	5.5
SbcPPr+	1	2	0	0	30	60	1.00	44
SbcPol	1	2	90	0	30	60	1.00	11
SbcR	1	2	150	0	150	180	0.60	50
SbcPPn = 0	1	0	0	0	30	60	1.00	11
SbcRn = 0	1	0	150	0	150	180	0.60	50
			G–G mergers					
G3PP	1	2	−30	0	30	60	0.95	13.6
G2PP	1	2	−30	0	30	60	0.95	3.8
G1PP	1	2	−30	0	30	60	0.95	3.0
G0PP	1	2	−30	0	30	60	0.95	2.2
G3PPn = 0	1	0	−30	0	30	60	0.95	13.6
G2PPn = 0	1	0	−30	0	30	60	0.95	3.8
G1PPn = 0	1	0	−30	0	30	60	0.95	3.0
G0PPn = 0	1	0	−30	0	30	60	0.95	2.2

[a]The numerical resolution of simulation is xN_{part}, where N_{part} is given in Table 1. [b]Supernova feedback polytropic index n where $P \propto \rho^{1+(n/2)}$ in star-forming regions. [c]Initial orientation of galaxy 1 with respect to the plane of the orbit in spherical coordinates, where $\theta = \arctan(\sqrt{x^2 + y^2}/z)$ and $\phi = \arctan(y/x)$. [d]Initial orientation of galaxy 2. [e]Eccentricity of the orbit, where a parabolic orbit has $e = 1$. [f]Pericentric distance of the initial orbit.

2.4 Galaxy merger parameters

Each of the galaxy merger simulations presented here are mergers of identical equal-mass galaxies; mergers of unequal-mass galaxies will be presented in a later paper. The Sbc–Sbc merger simulation parameters are selected to probe a range of different merger orientations and orbits (Table 2), including parabolic orbits with roughly prograde–prograde (SbcPP), prograde–retrograde (SbcPR), retrograde–retrograde (SbcRR) and prograde–polar orientations (SbcPol), parabolic prograde–prograde mergers with very small/large pericentric distances (SbcPPr−, SbcPPr+), and a highly radial orbit with prograde–retrograde orientation (SbcR). For most of the simulations, the galaxy orbits are initialized to be parabolic with the given pericentric distance; as the simulations progress, the galaxies lose angular momentum because of dynamical friction and eventually merge. The galaxies in the radial orbit simulation (SbcR) start out nearly at rest, so the pericentric distance and eccentricity

have little physical meaning in this case. The G–G merger simulations were all run with the same orientation (prograde–prograde) and slightly subparabolic orbits (eccentricity = 0.95) to probe the effect of varying total mass (G3PP, G2PP, G1PP, G0PP; Table 2). Subparabolic orbits were chosen so that the lower mass mergers (G1, G0) would merge in less than 2 Gyr. This choice will affect the close pair time-scales, but is unlikely to affect the morphological disturbance time-scales which peak at the first pass and final merger (see Section 4.6 for discussion).

The simulations only include feedback from supernovae. Most of these Sbc simulations were run with the 'stiff' $n = 2$ supernova feedback equation of state; the Sbc prograde–prograde merger and radial orbit merger were run with the isothermal $n = 0$ supernova feedback equation of state as well (SbcPPn = 0, SbcRn = 0). To test the simulations for convergence, the Sbc prograde–prograde merger was also run with four and ten times as many particles as our typical simulations (SbcPP×4, SbcPP×10). All of the G–G simulations were run with both supernova feedback models. Although feedback from an AGN may be important for the properties of the merger remnants, such feedback is not expected to affect the large-scale merger properties and morphology until after the coalescence of the nuclei. Such feedback is driven by a rapidly accreting AGN which may appear as an optically luminous quasar during the end stages of the merger. Incorporating a quasar into the radiative transfer code poses a number of technical challenges and is beyond the scope of this paper, but will be included in a future version of SUNRISE. As we discuss in Section 5, the exclusion of AGN feedback effects will not affect the morphological disturbance time-scales calculated here.

3 ANALYSIS

We replicate the observations and measurements of real galaxy mergers as closely as possible. Our simulations produce multiwavelength images of galaxy mergers including the effects of dust and star formation. Most current morphological measurements of the evolution of the galaxy merger rate are done in the rest-frame *B* or SDSS *g* (e.g. Conselice et al. 2003; Lotz et al. 2008). This is because high spatial resolution rest-frame 4000–5000 Å imaging can be done for local galaxies from the ground, for $z \sim 1$ galaxies with the *Hubble Space Telescope* (*HST*) Advanced Camera for Surveys (ACS), and for $z \leq 3$ galaxies with the *HST* Near-Infrared Camera and Wide Field Camera 3. Therefore we focus on SDSS *g* morphologies for purposes of this paper, as these simulations can be used to calibrate the morphologies of galaxies currently observed at $0 < z < 3$. In the following section we describe how the simulated SDSS *g* images are degraded and analysed to match real galaxy morphology measurements.

3.1 Image degradation

The SDSS *g* images are produced by SUNRISE for each simulation for 11 isotropically positioned viewpoints as a function of time from ~ 0.5 Gyr prior to the first pass to ≥ 1 Gyr after the final coalescence in ~ 30–250 Myr time-steps depending on the merger state. The field of view of the output images ranges from 200 kpc during the initial stages and period of maximal separation to 100 kpc during the first pass, final merger and post-merger stages. The intrinsic resolution of the output SUNRISE *g*-band images is 333 pc.

The images output by SUNRISE have no background sky noise and no seeing effects, although they do have particle noise and Monte Carlo Poisson noise. We degrade these images to simulate real data,

but do not attempt to mimic a particular set of galaxy survey observations. The measured morphology is dependent on the observed spatial resolution and signal-to-noise ratio (S/N) to the extent that low spatial resolution (>500 pc per resolution element) and low S/N (average S/N per pixel < 3–5) introduce biases in the morphology values. However, above these limits, measured morphologies are not dependent on spatial resolution or S/N (LPM04). We rebin the images to 105 pc pixel^{-1} and convolve the images with a Gaussian function with a full width at half-maximum (FWHM) = 400 pc. This was done to simulate the effect of seeing but maintain as high spatial resolution as possible. The values where chosen to match the SDSS with 1.5-arcsec seeing, 0.396 arcsec pixel^{-1} plate scale for a galaxy at a distance such that 1.5 arcsec ~ 400 pc. We also add random Poisson noise background to simulate sky noise but scale this noise to maintain a high S/N for the galaxies (>20 pixel^{-1} within the Petrosian radius). Our choice to simulate images with spatial resolution <400 pc per resolution element and S/N per pixel >20 means that our results here can be generally compared to any rest-frame ~ 4700 Å morphological study with sufficient spatial resolution and S/N. This corresponds to galaxies with a distance modulus <35.0 observed from the ground with a seeing point spread function (PSF) FWHM ~ 0.8 arcsec or galaxies at $z < 0.25$ observed with *HST* ACS and a PSF FWHM ~ 0.14 arcsec. In Section 4.2 we discuss how the results presented here apply to high-redshift galaxies observed with *HST* at spatial resolutions ~ 1 kpc, where the morphological biases from spatial resolution can be important.

3.2 Morphology measurements

The degraded image for each snapshot and camera is treated as an independent observation with no prior information except for the central position of the two galaxies, which is used to track the galaxies' identities. Each image is run through an automated galaxy detection algorithm integrated into our IDL code. This algorithm is similar to but simpler than the detection and deblending algorithm of SEXTRACTOR (Bertin & Arnouts 1996), which is optimized for large images with many objects but is ill suited for images of one or two objects. The image is smoothed by a ~ 4 kpc boxcar and initial segmentation maps of galaxies are determined based on a fixed surface brightness threshold equal to $2\sigma_{noise}$. The number of objects detected in the 2σ threshold map is compared to the number of objects detected in a 15σ threshold map. If more than one object larger than the smoothing length is detected in either map, a deblending algorithm is applied. The largest objects detected in the high-threshold map are grown using an image dilation algorithm (the IDL DILATE function) and a 5×5 pixel square-shaped operator, with a limiting surface brightness set to the 2σ threshold. The deblending algorithm adopted here results in similar segmentation maps to those used in LPM04 for the sample of local mergers.

If the centres of the merging galaxies are less than 10 kpc apart, they are generally detected as a single object. If two distinct galaxies are detected, the detection segmentation maps are used to mask out the other galaxy while each galaxy's morphology is measured. The output segmentation maps are visually inspected. Occasionally, the detection algorithm will assign a tidal dwarf galaxy as a second primary galaxy or fail to adequately mask out the secondary galaxy. In these cases, the masking is done by hand and the morphology code is rerun. For this paper, we ignore the properties of any tidal dwarfs produced in the merger and focus only on the merging galaxies and their remnants.

The centres of each galaxy are estimated by minimizing the second-order moment of the pixels assigned to the detection

segmentation map, and ellipticities and position angles are determined using the IDL task FIT_ELLIPSE (Fanning 2002). The projected separation R_{proj} is measured when two galaxies are detected. The initial guesses at the centre, ellipticity and position angle are then used to calculate the Petrosian radii in circular and elliptical apertures, concentration, asymmetry, clumpiness, the Gini coefficient and the second-order moment of the brightest 20 per cent of the light (see LPM04 and Conselice 2003 for further details).

The Petrosian radius is defined as the radius r_p at which the ratio of the surface brightness at r_p to the mean surface brightness within r_p is equal to a fixed value, i.e.

$$\eta = \frac{\mu(r_p)}{\bar{\mu}(r < r_p)}, \tag{1}$$

where η is typically set to 0.2 (Petrosian 1976). Because the Petrosian radius is based on a curve of growth, it is largely insensitive to variations in the limiting surface brightness and S/N of the observations.

Concentration is defined in slightly different ways by different authors, but the basic function measures the ratio of light within a circular inner aperture to the light within an outer aperture. We adopt the Bershady, Jangren & Conselice (2000) definition as the ratio of the circular radii containing 20 and 80 per cent of the 'total flux':

$$C = 5 \log 10 \left(\frac{r_{80}}{r_{20}} \right), \tag{2}$$

where r_{80} and r_{20} are the circular apertures containing 80 and 20 per cent of the total flux, respectively. For comparison to the most recent studies of galaxy concentration, we use Conselice's (2003) definition of the total flux as the flux contained within $1.5r_p$ of the galaxy's centre (as opposed to Bershady's definition as the flux contained within $2r_p$). For the concentration measurement, the galaxy's centre is that determined by the asymmetry minimization (see below). Bulge-dominated early-type galaxies generally have high concentrations ($C \sim 4$–6), while late-type discs have low concentrations ($C \sim 2$–3). Ongoing mergers may show very low concentrations or very high concentrations depending on the merger stage and the brightness of the central starburst.

The asymmetry parameter A quantifies the degree to which the light of a galaxy is rotationally symmetric. A is measured by subtracting the galaxy image rotated by $180°$ from the original image (Abraham et al. 1994; Conselice, Bershady & Jansen 2000):

$$A = \sum_{i,j} \frac{|I(i,j) - I_{180}(i,j)|}{|I(i,j)|} - B_{180}, \tag{3}$$

where I is the galaxy's image and I_{180} is the image rotated by $180°$ about the galaxy's central pixel, and B_{180} is the average asymmetry of the background. A is summed over all pixels within $1.5r_p$ of the galaxy's centre. The central pixel is determined by minimizing A. The asymmetry due to the noise must be corrected for, and it is impossible to reliably measure the asymmetry for very low-S/N images (LPM04). Objects with very smooth elliptical light profiles have low asymmetries ($A < 0.05$). Galaxies with spiral arms are more asymmetric ($A \sim 0.1$–0.2), while extremely irregular and merging galaxies are often highly asymmetric ($A > 0.35$).

The smoothness parameter S has been developed by Conselice (2003), inspired by the work of Takamiya (1999), in order to quantify the degree of small-scale structure. The galaxy image is smoothed by a boxcar of given width and then subtracted from the original image. The residual is a measure of the clumpiness due to features such as compact star clusters. In practice, the smoothing

scalelength is chosen to be a fraction of the Petrosian radius:

$$S = \sum_{i,j} \frac{|I(i,j) - I_S(i,j)|}{|I(i,j)|} - B_S, \tag{4}$$

where I_S is the galaxy's image smoothed by a boxcar of width $0.25r_p$, and B_S is the average smoothness of the background. Like A, S is summed over the pixels within $1.5\,r_p$ of the galaxy's centre. However, because the central regions of most galaxies are highly concentrated, the pixels within a circular aperture equal to the smoothing length $0.25\,r_p$ are excluded from the sum. S is correlated with recent star formation (Conselice 2003).

The Gini coefficient G is a statistic based on the Lorenz curve, the rank-ordered cumulative distribution function of a population's wealth or, in this case, a galaxy's pixel values (Abraham et al. 2003). The Lorenz curve is defined as

$$L(p) = \frac{1}{\bar{X}} \int_0^p F^{-1}(u)\mathrm{d}u, \tag{5}$$

where p is the percentage of the poorest citizens or faintest pixels, $F(x)$ is the cumulative distribution function and $\bar{X}$ is the mean over all (pixel flux) values X_i (Lorenz 1905). The Gini coefficient is the ratio of the area between the Lorenz curve and the curve of 'uniform equality' [where $L(p) = p$] to the area under the curve of uniform equality ($=1/2$). For a discrete population, the Gini coefficient is defined as the mean of the absolute difference between all X_i:

$$G = \frac{1}{2\bar{X}n(n-1)} \sum_{i=1}^{n} \sum_{j=1}^{n} |X_i - X_j|, \tag{6}$$

where n is the number of people in a population or pixels in a galaxy. In a completely egalitarian society, G is zero, and if one individual has all the wealth, G is unity. A more efficient way to compute G is to first sort X_i into increasing order and calculate

$$G = \frac{1}{|\bar{X}|n(n-1)} \sum_{i}^{n} (2i - n - 1)|X_i| \tag{7}$$

(Glasser 1962). G is high for objects with very bright nuclei ($G \sim 0.6$), whether those galaxies are highly concentrated ellipticals or mergers with multiple bright nuclei. It is low for objects with more uniform surface brightness, such as late-type discs ($G \sim 0.4$).

Because G is very sensitive to the ratio of low surface brightness to high surface brightness pixels, G must be measured within a well-defined segmentation map. For the purposes of measuring G and M_{20}, we have chosen to assign pixels to the galaxy based on the surface brightness at the Petrosian radius as measured in elliptical apertures (LPM04; see Abraham et al. 2007 for a similar approach). Note that the resulting segmentation map is not elliptical, but rather traces the isophote that matches the mean surface brightness at the elliptical Petrosian radius. The Petrosian radius is a reproducible quantity that is relatively independent of S/N and surface brightness dimming effects (LPM04). Designating galaxy pixels based on S/N cuts (e.g. Law et al. 2007) will result in unreliable G values. This is because galaxies with the same 'shape' or 'morphology' but differing luminosities will have different measured G values when S/N is used to define the galaxy pixels. For example, a low surface brightness exponential disc will have fewer low surface brightness pixels assigned to its segmentation map than a morphologically identical high surface brightness exponential disc, resulting in a lower G for the low surface brightness disc. Moreover, G values measured within segmentation maps based on S/N cuts are not repeatable because the measured G will depend as much on the noise properties of the observations as the intrinsic galaxy properties. The

results presented in this paper are robust to these effects because the pixel maps used to measure G are based on the surface brightness at the Petrosian radius.

The total second-order moment M_{tot} is the flux in each pixel, f_i, multiplied by the squared distance to the centre of the galaxy, summed over all the galaxy pixels assigned by the segmentation map:

$$M_{tot} = \sum_i^n M_i = \sum_i^n f_i \left[(x_i - x_c)^2 + (y_i - y_c)^2 \right], \qquad (8)$$

where x_c, y_c is the galaxy's centre. The centre is computed by finding x_c, y_c such that M_{tot} is minimized. The second-order moment of the brightest regions of the galaxy traces the spatial distribution of any bright nuclei, bars, spiral arms, and off-centre star clusters. M_{20} is defined as the normalized second-order moment of the brightest 20 per cent of the galaxy's flux. To compute M_{20}, we rank-order the galaxy pixels by flux, sum M_i over the brightest pixels until the sum of the brightest pixels equals 20 per cent of the total galaxy flux, and then normalize by M_{tot}:

$$M_{20} \equiv \log_{10} \left(\frac{\sum_i M_i}{M_{tot}} \right) \quad \text{while} \quad \sum_i f_i < 0.2 f_{tot}. \qquad (9)$$

Here f_{tot} is the total flux of the galaxy pixels identified by the segmentation map and f_i are the fluxes for each pixel i, ordered such that f_1 is the brightest pixel, f_2 is the second brightest pixels and so on. The normalization by M_{tot} removes the dependence on total galaxy flux or size. M_{20} always has a value <0. M_{20} is anticorrelated with C for normal galaxies, with low values for early-type galaxies ($M_{20} \leq -2$) and intermediate values for late-type galaxies ($M_{20} \sim -1.5$). Mergers with multiple nuclei have high M_{20} values (≥ -1).

3.3 Definition of merger stages

From the true three-dimensional separations of the galaxy nuclei, we determine the time-step of the closest approach during the first pass (t_{fp}), maximal separation after the first pass (t_{max}), and final merger of the nuclei where $\delta r < 1 \, kpc$ (t_{merg}). These times are given in Table 3 for each simulation. Based on these events, we define six merger stages: pre-merger, first pass, maximal separation, final merger, post-merger and merger remnant. The 'pre-merger' stage is from $t = 0$ to $0.5 \, t_{fp}$. The 'first pass' stage encompasses the first pass and starts at $0.5 \, t_{fp}$ and ends at $0.5 \, (t_{fp} + t_{max})$. The 'maximal separation' stage starts at $0.5 \, (t_{fp} + t_{max})$ and ends at $0.5 \, (t_{max} + t_{merg})$. The 'merger' stage starts at $0.5 \, (t_{max} + t_{merg})$ and ends at $t_{merg} + 0.5 \, Gyr$. The 'post-merger' stage is defined as between $t_{merg} + 0.5 \, Gyr$ and $t_{merg} + 1.0 \, Gyr$, while the 'remnant' stage is at times more than 1 Gyr after the merger event ($t_{merg} + 1.0 \, Gyr$). We show composite SDSS $u - r - z$ images for each of these stages for a prograde–prograde Sbc merger simulation as viewed face-on (Fig. 1) and edge-on (Fig. 2).

3.4 Merger classification and time-scales

In Fig. 3, we show the empirical criteria for merger classification via $G - M_{20}$, $G - A$ and $C - A$ morphologies for local samples of visually classified galaxies (LPM04). All three morphological merger criteria are based on the Borne et al. (2000) observations of local ultraluminous infrared galaxies (ULIRGs), a subset of which have been shown to be gas-rich mergers with mass ratios between 1:3 and 1:1 (Dasyra et al. 2006). LPM04 found that ULIRGs visually classified as mergers could be distinguished from the sequence of normal Hubble type galaxies with

$$G > -0.115 \, M_{20} + 0.384 \qquad (10)$$

or

$$G > -0.4A + 0.66 \text{ or } A \geq 0.4. \qquad (11)$$

Asymmetry alone is also often used to classify merger candidates. The calibration of local mergers by Conselice (2003) finds the

Table 3. Merger stages.

Simulation	First pass (Gyr)	Maximum separation (Gyr)	Merger (Gyr)	Post-merger (Gyr)	Remnant (Gyr)
		Sbc–Sbc mergers			
SbcPP×10	0.59	1.03	1.66	2.16	2.66
SbcPP×4	0.59	1.03	1.71	2.21	2.71
SbcPP	0.59	1.03	1.71	2.21	2.71
SbcPR	0.59	1.08	1.71	2.21	2.71
SbcRR	0.59	1.12	1.71	2.21	2.71
SbcPPr−	0.59	0.88	1.37	1.87	2.37
SbcPPr+	0.68	1.91	3.76	4.26	4.76
SbcPol	0.59	1.17	2.00	2.50	3.00
SbcR	1.28	1.47	1.70	2.20	2.70
SbcPPn = 0	0.59	1.03	1.71	2.21	2.71
SbcRn = 0	1.28	1.42	1.66	2.16	2.66
		G–G mergers			
G3PP	0.85	1.47	2.44	2.93	3.43
G2PP	0.40	0.70	1.24	1.74	2.24
G1PP	0.45	0.68	1.24	1.74	2.24
G0PP	0.55	0.88	1.42	1.92	2.41
G3PPn = 0	0.83	1.37	2.40	2.90	3.40
G2PPn = 0	0.39	0.68	1.17	1.67	2.17
G1PPn = 0	0.45	0.68	1.24	1.74	2.24
G0PPn = 0	0.54	0.83	1.32	1.82	2.32

The time since the start of the simulation is given for each event that defines a particular merger stage (see Section 3.3 for definitions).
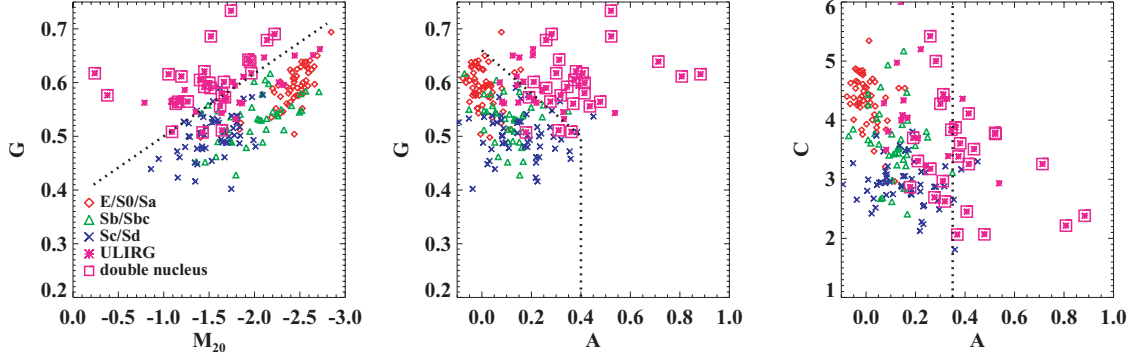
Figure 3. $G - M_{20}$, $G - A$ and $C - A$ relations for local galaxies measured by LPM04. Empirically, normal galaxies lie below the dashed lines in the $G - M_{20}$ and $G - A$ plots and to the left-hand side of the dashed line in the $C - A$ plot. Mergers are identified as galaxies which lie above and/or to the right-hand side of these divisions. While 90 per cent of local ULIRGs show visual signs of merger activity, ULIRGs with double nuclei show the strongest signatures in quantitative morphology.

following merger criterion:

$$A \geq 0.35. \qquad (12)$$

These are the merger criteria used to calculate the morphological observability time-scales throughout most of this paper.

Galaxies at higher redshift cannot be imaged at as high spatial resolution as local galaxies even when observed with *HST*. The measured morphologies of galaxies at $z > 0.25$ imaged with *HST* will have non-negligible biases as a result of this lower spatial resolution (LPM04). Therefore the merger criteria have been adjusted to account for these biases in *HST* data by Conselice et al. (2003), Conselice, Blackburne & Papovich (2005) and Lotz et al. (2008). For $z < 1.2$ galaxies observed with *HST* ACS Wide Field Camera at rest-frame ~ 4000 Å, the revised $G - M_{20}$ merger classification is

$$G > -0.14\, M_{20} + 0.33 \qquad (13)$$

(Lotz et al. 2008). Conselice et al. (2005) find that decreased spatial resolution and surface brightness dimming at $z > 0.5$ can lower the measured A in irregular galaxies by 0.05–0.15 (also Shi, in preparation). In Section 4.2, we find a median offset of -0.05 for A when our simulations are convolved to match the spatial resolution of *HST* ACS WFC F814W observations at $z \sim 1$. Therefore we suggest a revised merger criterion for $G - A$ and A for *HST* observations of high-redshift galaxies as follows:

$$G > -0.4A + 0.68 \text{ or } A \geq 0.35 \qquad (14)$$

and

$$A \geq 0.30. \qquad (15)$$

We will use these merger criteria in Section 4.2 for the simulations convolved to match *HST* ACS observations of galaxies at $z \sim 1$.

Close kinematic pairs are also probable merging systems. Recent studies of local kinematic pairs have selected objects with $5 < R_{\mathrm{proj}} < 20\, h^{-1}$ kpc (Patton et al. 2002; de Propris et al. 2005) and relative velocities $\leq 500\,\mathrm{km\,s^{-1}}$, while studies of pairs out to $z \sim 1.4$ has chosen objects with $10 < R_{\mathrm{proj}} < 30$, 50 and $100\, h^{-1}$ kpc and relative velocities $\leq 500\,\mathrm{km\,s^{-1}}$ (Lin et al. 2004). We assume $h = 0.7$ and we estimate the time-scales during which merging galaxies can be found as separate objects within $5 < R_{\mathrm{proj}} < 20$, $10 < R_{\mathrm{proj}} < 30$, $10 < R_{\mathrm{proj}} < 50$ and $10 < R_{\mathrm{proj}} < 100\, h^{-1}$ kpc. The simulated merging galaxies always have relative velocities $< 500\,\mathrm{km\,s^{-1}}$.

The galaxy merger rate Γ is defined as the number of ongoing merger events per unit volume ϕ_{merg} divided by the time T_{merg} for the merger to occur from the initial encounter to the final coalescence:

$$\Gamma = \frac{\phi_{\mathrm{merg}}}{T_{\mathrm{merg}}}. \qquad (16)$$

However, the number density of galaxies identified morphologically as galaxy mergers ϕ'_{merg} will depend on the time-scale T'_{merg} during which the merger can be observed given the method used to identify it such that

$$\phi'_{\mathrm{merg}} = \phi_{\mathrm{merg}} \frac{T'_{\mathrm{merg}}}{T_{\mathrm{merg}}}. \qquad (17)$$

Therefore the galaxy merger rate Γ can be calculated from the observed number density of galaxy merger candidates ϕ'_{merg} as follows:

$$\Gamma = \frac{\phi'_{\mathrm{merg}}}{T_{\mathrm{merg}}} \frac{T_{\mathrm{merg}}}{T'_{\mathrm{merg}}} = \frac{\phi'_{\mathrm{merg}}}{T'_{\mathrm{merg}}}. \qquad (18)$$

The effective observability time-scale T' given in equation (18) is a weighted average of the time-scales over all likely merger mass ratios, gas fractions and orbital parameters. We do not calculate this global observability time-scale here because this may require a cosmological model for the distribution of galaxy merger properties if the observability time-scale for a given method varies strongly. Instead, we present the first steps towards calculating the global observability time-scales by exploring the dependence of the time-scales on a wide range of galaxy merger properties.

We calculate each simulation's average observability time-scale for the $G - M_{20}$, $G - A$ and A criteria given above by averaging the results of the 11 isotropic viewpoints. Hereafter we drop the prime notation and refer to the observability time-scale for each simulation as T. Because we wish to determine the number density of merger events rather than the number of galaxies undergoing a merger, galaxies that have not yet merged but identified morphologically as merger candidates are weighted accordingly. The time that each pre-merger galaxy is morphologically disturbed is summed (not averaged) to the time that the post-merger system appears disturbed. No such weighting is done for the close pair time-scales as this factor is generally included in the merger rate calculation (e.g. Patton et al. 2000):

$$\Gamma = 0.5\, \phi\, N_c\, p(\mathrm{merg})\, T_{\mathrm{pair}}^{-1}, \qquad (19)$$

where ϕ is the number density of galaxies within the magnitude range of the observed pairs, N_c is the average number of companions

within the observed magnitude range per galaxy, $p(\text{merg})$ is the probability that a galaxy pair will merge, T_{pair} is the time-scale for which merging galaxies will meet the close pair criteria and 0.5 is the weighting factor that accounts for the double counting of pairs.

4 RESULTS

The equal-mass galaxy merger simulations span a wide range of physical properties. These include the relative orientations and orbital parameters of the merging galaxies, the gas fraction and scale-length, the assumed supernova feedback prescription and mass. In this section, we explore how important these physical parameters, the inclusion of dust and simulation resolution are to the predicted morphologies. We present the viewing-angle averaged observability time-scales for $G - M_{20}$, $G - A$ and A morphologies (Table 6) and close pair projected separations $R_{\text{proj}} < 20, 30, 50$ and $100\,h^{-1}$ kpc for each simulation (Table 7). Finally, the morphologies of the remnants observed 1 Gyr after the merger are calculated (Table 8).

For each simulation, we examine the projected separations R_{proj}, measured morphologies (G, M_{20}, C, A and S), and star formation rate per object as a function of time and merger stage for each simulation for all 11 viewpoints. The initial segmentation maps computed to identify each galaxy are used to compute the total star formation rate for each galaxy at each time-step and camera. In general we only examine the morphologies of the output images that include the effects of dust absorption and scattering. In Fig. 4, we show the evolution with time for the highest resolution prograde–prograde Sbc merger simulation, SbcPP×10. The merger stages are

colour-coded, with red for pre-merger, green for first pass, blue for maximal separation, orange for merger, magenta for post-merger and cyan for the remnant. The scatter at each time-step reflects the scatter in morphology with viewing angle. Before the final merger, the morphologies are measured separately for each galaxy (open diamonds and crosses). After the merger, the system is treated as a single object (open diamonds).

Most of the parabolic orbit mergers show trends of morphology and star formation rate with merger stage similar to the SbcPP×10 merger (Figs 4 and 5). Leading up to and including the first pass (green points), the morphologies become increasingly disturbed as tidal tails are formed and the galaxies overlap in projection. The star formation rate per object peaks at the first pass because the system appears as one object, but remains enhanced above the initial star formation rates as the galaxies approach their maximal separations (blue points). Dust starts to obscure star formation in the nuclei, lowering G and C and increasing M_{20}. Strong morphological disturbances are observed again at the final merger (orange points). The star formation rate per object reaches its peak at or just after the final merger and generally continues at high levels until ∼0.5–1 Gyr after the coalescence of the nuclei. In Fig. 5, we show the progression of the SbcPP×10 merger in $G - M_{20}$, $G - A$ and $C - A$ averaged over all viewing angles (top) and for all 11 cameras (bottom). The initial galaxies (red points) start with late-type disc morphologies in all three plots. The system become disturbed in $G - M_{20}$ space during the first pass (green points) and disturbed in $G - A$ and $C - A$ during the first pass and final merger (orange points). The post-mergers and remnants gradually end up with early-type disc morphologies in all three plots (cyan points).
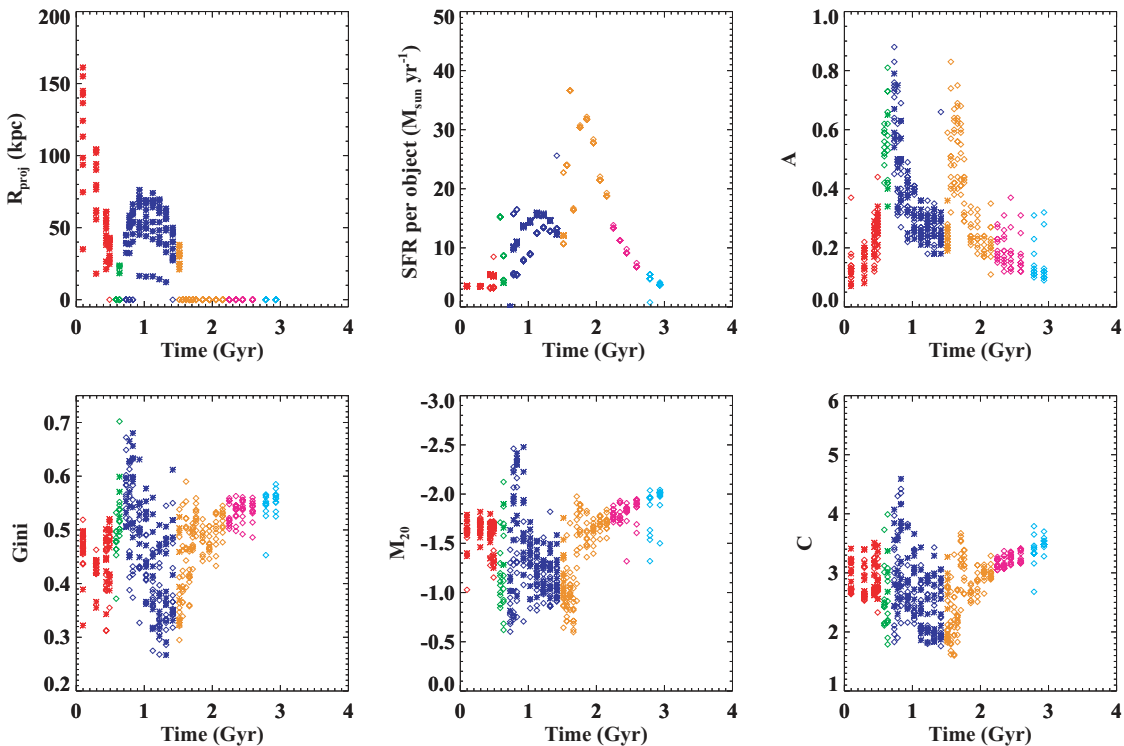
Figure 4. Time versus R_{proj}, star formation rate per object, A, G, M_{20} and C for the high-resolution prograde–prograde Sbc merger with stiff supernova feedback, including the effects of dust (SbcPP×10). Each merger stage is marked with a different colour (pre-merger: red, first pass: green, maximal separation: blue, final merger: orange, post-merger: magenta, remnant: cyan). Open diamonds are for the one merging galaxy and the merger remnant; crosses are for the other merging galaxy. The mergers show strong morphological disturbances and peaks in the star formation rate at the first pass (green points) and final merger (orange points).
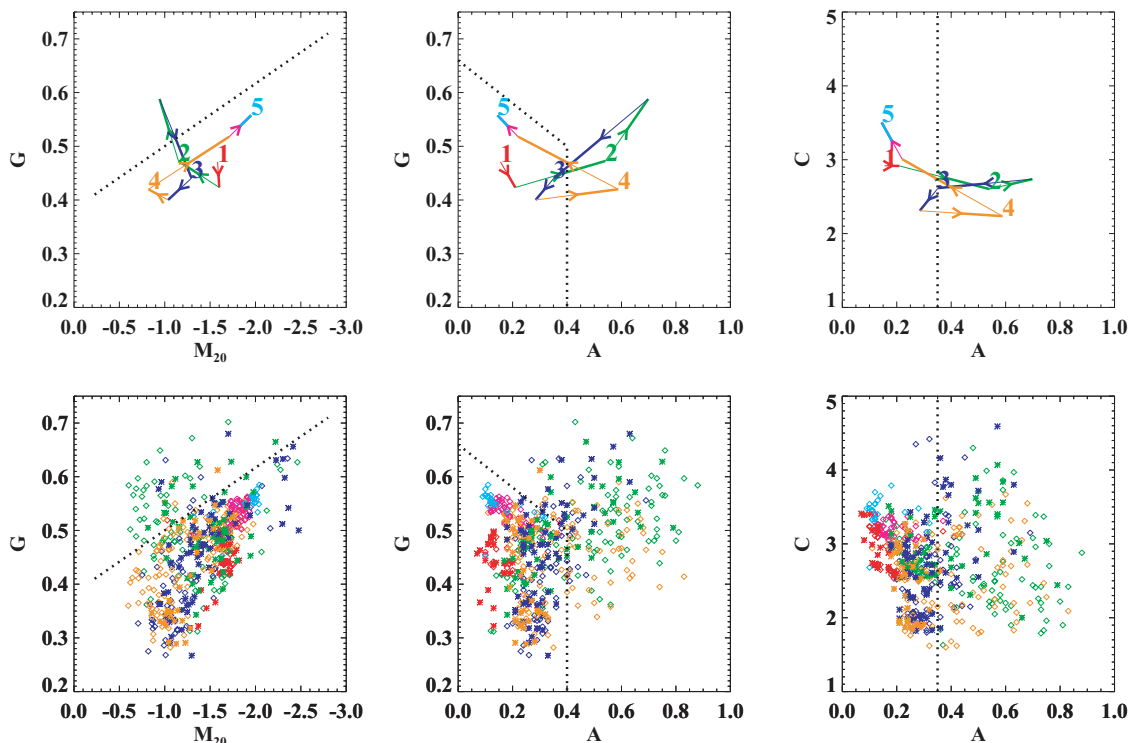
Figure 5. Top: Morphological evolutionary tracks in $G - M_{20}$, $G - A$ and $C - A$ space for the high-resolution prograde–prograde Sbc merger (SbcPP×10) averaged over all viewing angles. The initial galaxy (red), first pass (green), maximal separation (blue), final merger (orange) and last computed merger remnant (cyan) morphologies are labelled as 1–5, respectively. The black dashed lines show the empirical merger classification criteria from Fig. 3. Bottom: The morphologies for all the time-steps and cameras for the SbcPP×10 simulation. The merger stages are indicted by the different colours, as in Fig. 4. For this simulation, $G - M_{20}$ identifies SbcPP×10 mergers primarily at the first pass, while $G - A$ and A find mergers at both the first pass and final merger.

4.1 Numerical resolution

Most of our simulations were run with $\sim 10^5$ particles per galaxy, with gravitational softening lengths of 400 and 100 pc for the dark matter and baryonic particles, respectively (Table 1). The number of simulation particles affects both the spatial resolution of the simulation and the noise in the fluctuations of the gravitational potential. This number of particles was found to adequately recover the system-averaged star formation histories and remnant properties when compared to simulations with larger numbers of particles (Cox et al. 2006). Here we compare the time-dependent morphologies of the stiff supernova feedback prograde–prograde Sbc merger (SbcPP) to simulations run with 4 and 10 times as many particles (SbcPP×4 and SbcPP×10) to determine if the standard numerical resolution of the simulations is adequate also for analysing morphology. These higher numerical resolution simulations were processed by SUNRISE and the morphologies of the output SDSS *g* images were compared to the fiducial simulation at each time-step. The time evolution is slightly different in distinct simulation runs, so when the morphologies are rapidly changing, the morphologies, half-light radii ($R_{1/2}$) and galaxy separations may be significantly different for the different runs at a given time-step. However, for the majority of the simulation time-steps, differences in the morphologies will reflect the differing spatial resolution and the noise in the gravitational potentials of the simulations. We find no resolution dependence for the time-scales of close pair projected separations R_{proj}, and so we focus only on the morphologies in this section.

In Fig. 6, we plot the difference between the standard resolution simulation SbcPP and the highest resolution simulation SbcPP×10

as a function of time for all 11 viewing angles including the effects of dust. We find strong offsets in the half-light radii ($R_{1/2}$) and morphologies for a few time-steps immediately after the first pass at 0.6 Gyr and immediately before the final merger at 1.7 Gyr, as expected from small timing differences between the different simulations. For the majority of time-steps, the mean differences between G, C, and effective radii for the standard and high-resolution simulations are negligible but show significant scatter with viewing angle after the first pass. M_{20}, A and S do show systematic offsets particularly for the initial undisturbed galaxies ($t < 0.6$ Gyr; dashed vertical line in Fig. 6).

We compare the location of the brightest 20 per cent of the pixels for the standard resolution and high-resolution images of the initial discs in Fig. 7. Young star particles in the spiral arms of the initial galaxies dominate the morphologies because they are not adequately sampled in the fiducial simulations. Because star formation is implemented by creating star particles whose mass depends on the resolution of the simulation, the fiducial simulations have fewer and brighter star clusters. For isolated and pre-merger galaxies, most new star particle formation happens at star formation surface densities close to resolution of the output images ($\Sigma_{SFR} \sim 0.03\,\mathrm{M_\odot\,yr^{-1}\,kpc^{-2}}$, for $10^5\,\mathrm{M_\odot}$ new star particles, images with a spatial resolution ~ 400 pc, and O/B star lifetimes ~ 20 Myr; see also fig. 3 in Cox et al. 2006). Therefore the new stars are concentrated into a single particle within a single spatial resolution element, and the stochastic formation of individual star particles has a strong influence on the morphologies. As the numerical resolution is increased and the mass of a new star particle decreases, new stars are distributed over several particles. This decreases the
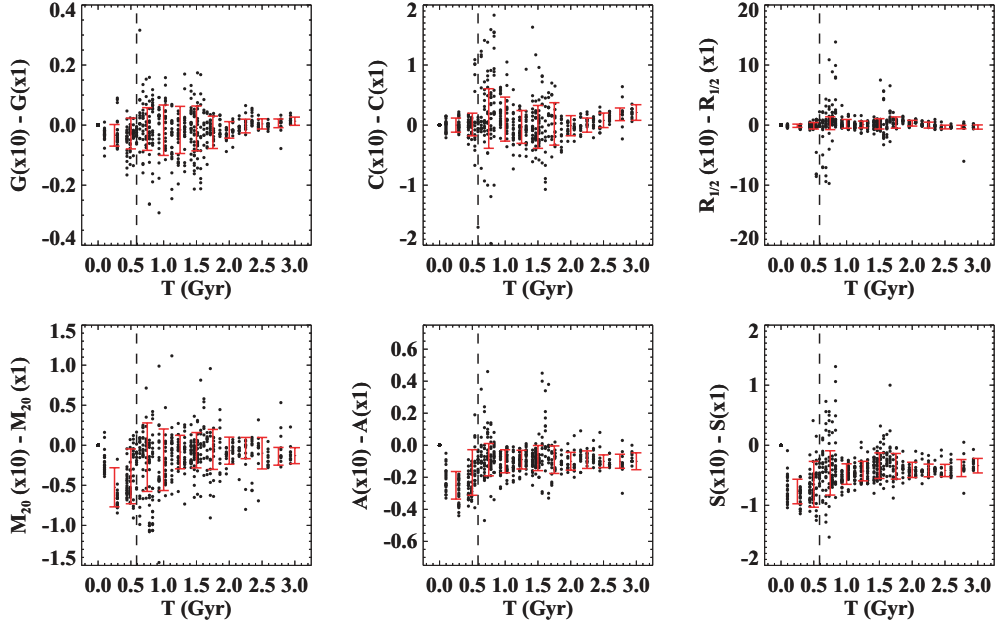
Figure 6. Δ morphology versus time for the prograde–prograde Sbc simulation run with $10\times$ (SbcPP$\times$10) and $1\times$ (SbcPP) the standard number of particles. The red error bars show the standard deviation of the morphology differences within 0.25 Gyr bins. Prior to 0.6 Gyr (dashed line), the low-resolution simulations has higher M_{20} and A values than the high-resolution simulation.
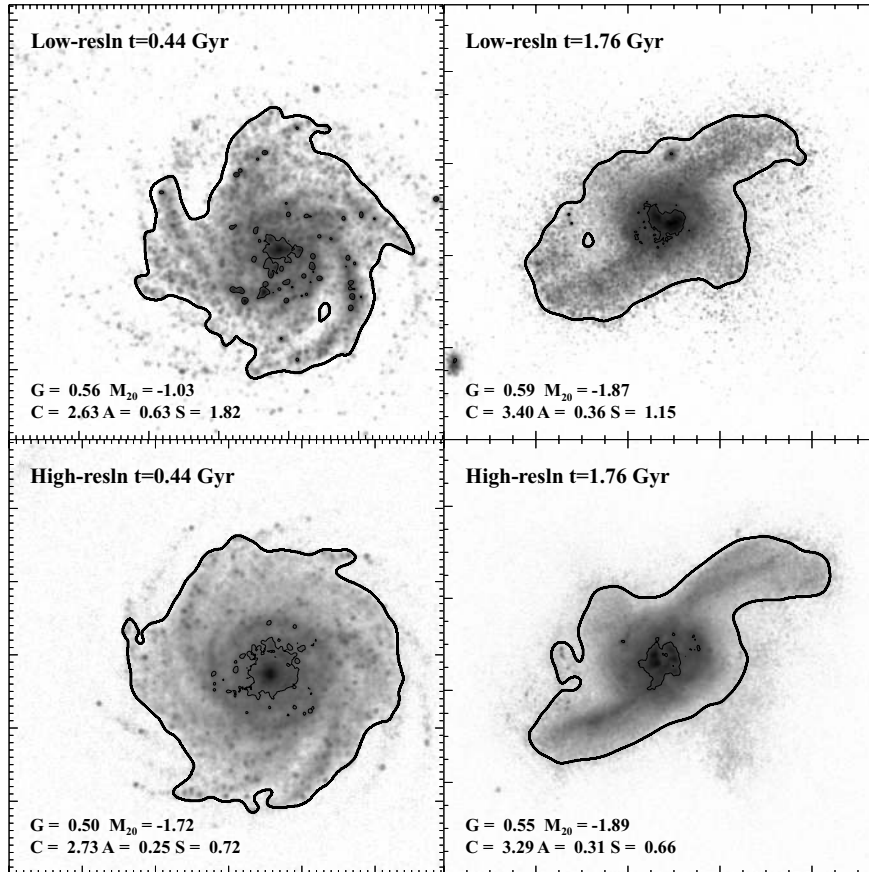
Figure 7. Top: SDSS g-band images for standard resolution simulation SbcPP at time = 0.44 and 1.76 Gyr. Bottom: Same for high numerical resolution SbcPP$\times$10 simulation. Thick contours show the segmentation maps used to compute G and M_{20}. The thin contours show the pixels containing brightest 20 per cent flux. Prior to the merger, the relatively low star formation surface densities result in new stars that are concentrated in a single particle for a given star-forming region in the standard resolution simulations, resulting in artificially high M_{20}, A and S values. During and after the merger, high star formation surface densities produce multiple new star particles per star-forming region, resulting in more consistent morphologies between the standard and high numerical resolution simulations.

Table 4. Morphological time-scales versus resolution.

Simulation	$T(G - M_{20})$ (Gyr)	$T(G - A)$ (Gyr)	$T(A)$ (Gyr)
	No corrections		
SbcPP×10	0.27 ± 0.13	0.95 ± 0.16	1.01 ± 0.14
SbcPP×4	0.30 ± 0.12	0.79 ± 0.17	0.82 ± 0.17
SbcPP	0.77 ± 0.15	2.12 ± 0.51	2.74 ± 0.30
	$t \geq 0.6\,\mathrm{Gyr}$		
SbcPP×10	0.26 ± 0.10	0.90 ± 0.14	0.94 ± 0.13
SbcPP×4	0.30 ± 0.11	0.78 ± 0.17	0.80 ± 0.15
SbcPP	0.56 ± 0.19	1.45 ± 0.31	1.94 ± 0.28
	$t \geq 0.6\,\mathrm{Gyr}; \delta M_{20} = -0.157; \delta A = -0.115$		
SbcPP	0.39 ± 0.16	0.78 ± 0.21	0.74 ± 0.17

PP = prograde–prograde; $\times 10 = 10\,N_{\mathrm{part}}$; $\times 4 = 4\,N_{\mathrm{part}}$.

typical surface brightness of the star-forming regions and the morphologies are less dominated by stochastic star particle formation. During the merger and remnant stages, most of the star formation happens at gas densities well above the numerical limit of the fiducial simulations (see fig. 8 in Cox et al. 2006). Therefore the new stars are already distributed over multiple particles for the fiducial simulations, and the morphologies are not dominated by stochastic new star particle formation (Fig. 7).

After the first pass, the standard resolution simulation continues to show small but significant offsets to higher M_{20}, A and S relative to the high-resolution simulation (Fig. 6). Even when we ignore the $t < 0.6\,\mathrm{Gyr}$ time-steps, we still find morphological disturbance time-scales twice as long for the standard resolution simulations (Table 4). We compute the mean offsets in $M_{20}(-0.157)$ and A (-0.115) between the standard and high-resolution simulations after the first 0.6 Gyr. We recompute the standard resolution merger time-scales ignoring the pre-merger initial galaxy morphologies

and correcting the morphologies by the mean offsets at t > 0.6 Gyr. These corrected time-scales are within 1σ of the high-resolution simulation merger time-scales, where 1σ is the standard deviation derived from the 11 viewing angles (Table 4). Given the large S offsets with simulation resolution, we do not include S in our analysis.

We compare the output morphologies of the $4\times$ and $10\times$ resolution simulations (SbcPP×4, SbcPP×10) to check that these simulations are resolved. Here the morphologies and time-scales agree quite well, even during pre-merger stage (Fig. 8, Table 4). This paper is a first attempt at computing the wavelength-dependent morphologies for a large parameter space upon which future studies can build. Therefore we choose to examine only time-steps after the pre-merger stage ($t > 0.6\,\mathrm{Gyr}$) and apply the same corrections for M_{20} and A when calculating the observability time-scales for the standard resolution simulations throughout this paper.

4.2 Image resolution

At $z > 0.25$, even galaxies observed with *HST* have images with worse spatial resolution than our fiducial resolution (400 pc per resolution element). As we discuss in Section 3 and show in LPM04, morphologies measured in images with spatial resolutions worse than 500 pc per resolution element have resolution-dependent biases. In principle, for images with low spatial resolution one should model the redshift and PSF-dependent biases for one's particular data set. However, the turnover in the angular size–redshift relation is such that the angular scale of galaxies does not change dramatically at $z > 0.6$. In order to determine if the time-scales calculated here can be applied to *HST* images of high-redshift galaxies, we measure the morphologies and time-scales of the high numerical resolution simulation SbcPP×10 tuned to match typical *HST* observations of galaxies at $z \sim 1$. We use the
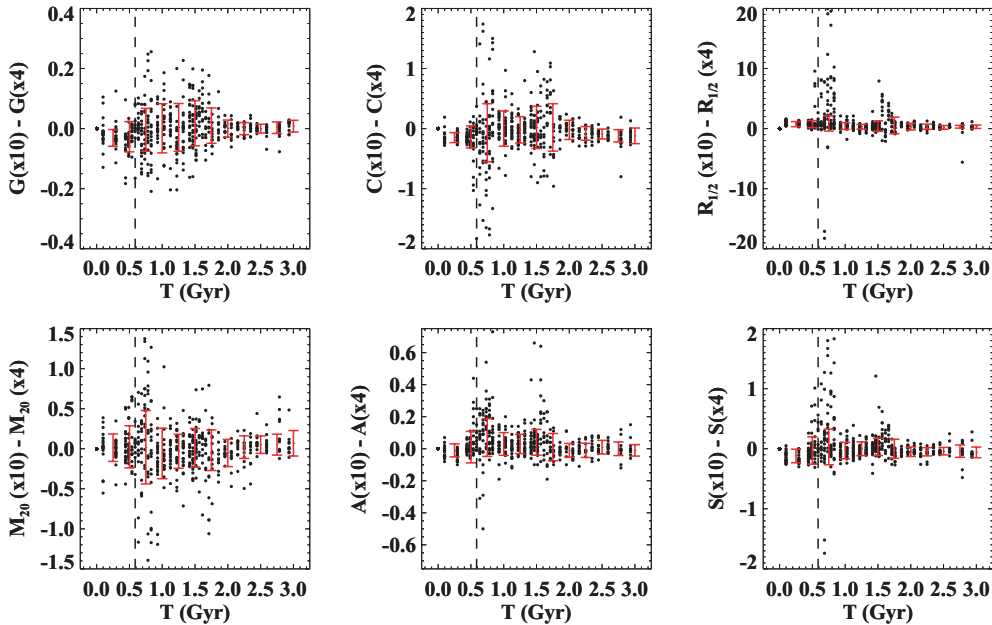
Figure 8. Δ morphology versus time for the prograde–prograde Sbc simulation run with $10\times$ (SbcPP×10) and $4\times$ (SbcPP×4) the standard number of particles. The red error bars show the standard deviation of the morphology differences within 0.25-Gyr bins. The morphologies of the initial galaxies agree well at all times, including the initial stages at $t < 0.6\,\mathrm{Gyr}$ (dashed line).
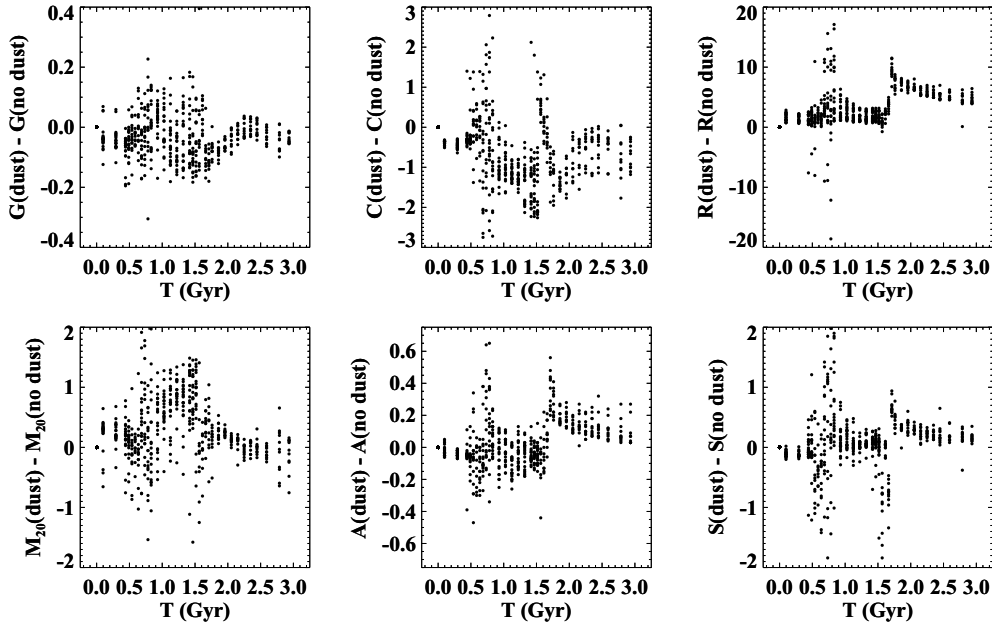
Figure 9. Δ morphology versus time for the high numerical resolution prograde–prograde Sbc merger (SbcPP×10) with and without the effects of dust extinction.

TINYTIM[1] software to calculate the PSF of ACS WFC in the F814W (wide *I*) filter. We scale the PSF FWHM (0.14 arcsec) to 1.1 kpc to match the angular scale at $z \sim 1$ and convolve the SbcPP×10 simulation images with this PSF.

The morphologies measured from these images show non-negligible offsets from the images convolved to 400 pc resolution for M_{20}, C and A. The median offsets calculated for all time-steps and viewing angles are $\delta G = -0.01 \pm 0.06$, $\delta M_{20} = -0.03 \pm 0.2$, $\delta C = +0.12 \pm 0.34$ and $\delta A = -0.05 \pm 0.06$. These offsets are consistent with the artificial redshift tests of real galaxies by LPM04 and Conselice et al. (2005). Without any corrections to the merger criteria given in equations (10)–(12), these shifts result in shorter observability time-scales [$T(G - M_{20}) = 0.14 \pm 0.12$ Gyr, $T(G - A) = 0.58 \pm 0.17$ Gyr, $T(A) = 0.47 \pm 0.17$ Gyr versus 0.26 ± 0.10, 0.90 ± 0.14 and 0.94 ± 0.13 Gyr, respectively].

If revised merger criteria of equations (13)–(15) (which take into account of the effect of decreased spatial resolution) are applied, then the derived time-scales are in better agreement with the higher spatial resolution images: $T(G - M_{20}) = 0.25 \pm 0.12$ Gyr, $T(G - A) = 0.70 \pm 0.17$ Gyr and $T(A) = 0.58 \pm 0.15$ Gyr. The pair time-scales are also ~200 Myr shorter than the fiducial resolution images. Although merging objects may be more difficult to detect at high redshift with *HST* observations, the ~200–300 Myr offsets in the asymmetry and pair time-scales are significantly less than the variations associated with the gas properties and merger orbital properties (Sections 4.3 and 4.4). We conclude that the time-scales presented here can be applied to *HST* observations of high-redshift galaxies without introducing uncertainties larger than those from the unknown distribution of merger properties.

4.3 Dust and viewing angle

The presence and distribution of dust has a strong effect on the measured morphologies starting at the first pass until after the final

merger. In Fig. 9, we plot the difference in the morphologies when dust is and is not included for SbcPP×10. During the merger, dust mitigates the effect of star formation on the morphologies. The presence of dust lowers G and C and increases M_{20} because the brightest star-forming regions near the centres of the merging galaxies are enshrouded. The $G - M_{20}$ observability time-scale is most strongly affected by the presence of dust, and is a factor of 2 less when dust is included (Table 6). The $G - A$ and A time-scales are relatively independent of extinction because the measured asymmetry is less affected (Fig. 9). The close pair time-scales are unchanged, as the measured positions and projected separations are unaffected by dust extinction. Most of the gas-rich simulations presented here continue to form stars at a significant rate ($>2\,\mathrm{M_\odot\,yr^{-1}}$) at 1 Gyr after the merger of the nuclei, and retain significant amounts of gas and dust. If the dust is ignored, the remnants appear highly concentrated and relatively blue (Table 8). With dust, the remnants appear less concentrated with lower C, G and higher M_{20} and A values because the central star formation is obscured and dust increases the asymmetry of the merger remnant (Table 8).

The morphologies observed in SDSS *g* band depend on the viewing angle, in part because the dust lanes will preferentially absorb blue light along certain lines of sight. Projection effects and the relative orientations of the merging galaxies will also change the projected separations and observed morphology. The scatter in the morphology at a given time-step in Fig. 4 is the result of the different viewing angles for the 11 different SUNRISE cameras. This scatter is largest immediately after the first pass and during the final merger when the system is most asymmetric, and is smallest for the merger remnant which is more spherically symmetric. We show the dependence of the measured morphologies on viewing angle in Fig. 10 for the initial disc galaxies and the final remnant. The measured morphologies do not change significantly with viewing angle for the initial galaxies. The remnant shows significantly higher M_{20}, A and S values when the final dust lane and star-forming disc is viewed edge-on (cameras 3 and 4). In Table 5, we give the SbcPP×10 simulation merger time-scales for each viewing angle including the effect of dust. The standard deviation over all 11

---

[1] J. Krist and R. Hook; http://www.stsci.edu/hst/software/tinytim.
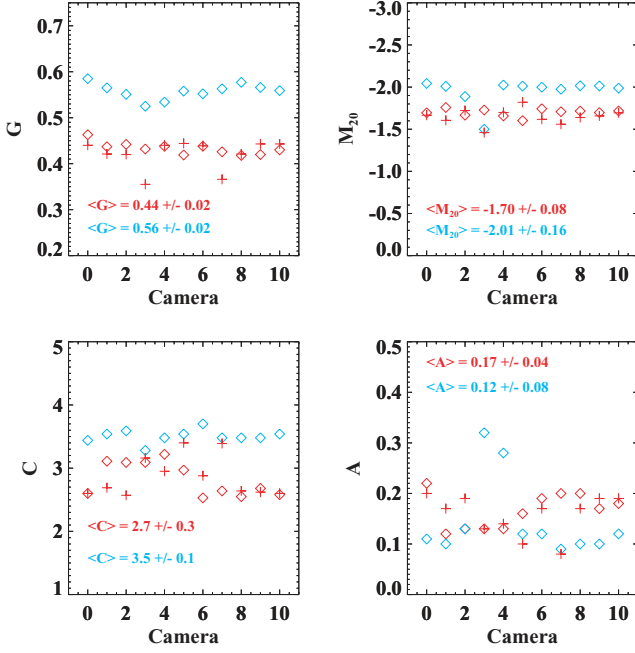
Figure 10. Morphology as a function of viewing angle for the high-resolution prograde–prograde Sbc merger (SbcPP×10). The red symbols show the initial galaxy morphologies and the cyan symbols show the final remnant morphologies. The measured morphologies of the initial disc galaxies do not change significantly with viewing angle. The merger remnant shows significantly higher M_{20} and A values when the dust lane is viewed edge-on (cameras 3 and 4).

viewing angles is $\sim$100 Myr for $T(G - M_{20})$, $T(G - A)$ and $T(A)$. The close pair time-scales and projected separations R_{proj} also depend on viewing angle, as the galaxies will have smaller R_{proj} along some lines of sight. The close pair time-scales have a standard deviation $\sim$200 Myr over the 11 different viewing angles.

4.4 Orientation and orbital parameters

We examine the importance of the orbits and relative orientations of the merging galaxies to their morphologies. Sbc mergers initialized on parabolic orbits with pericentric distances $R_{peri} = 11$ kpc and stiff feedback were simulated with roughly prograde–prograde (SbcPP), prograde–retrograde (SbcPR),
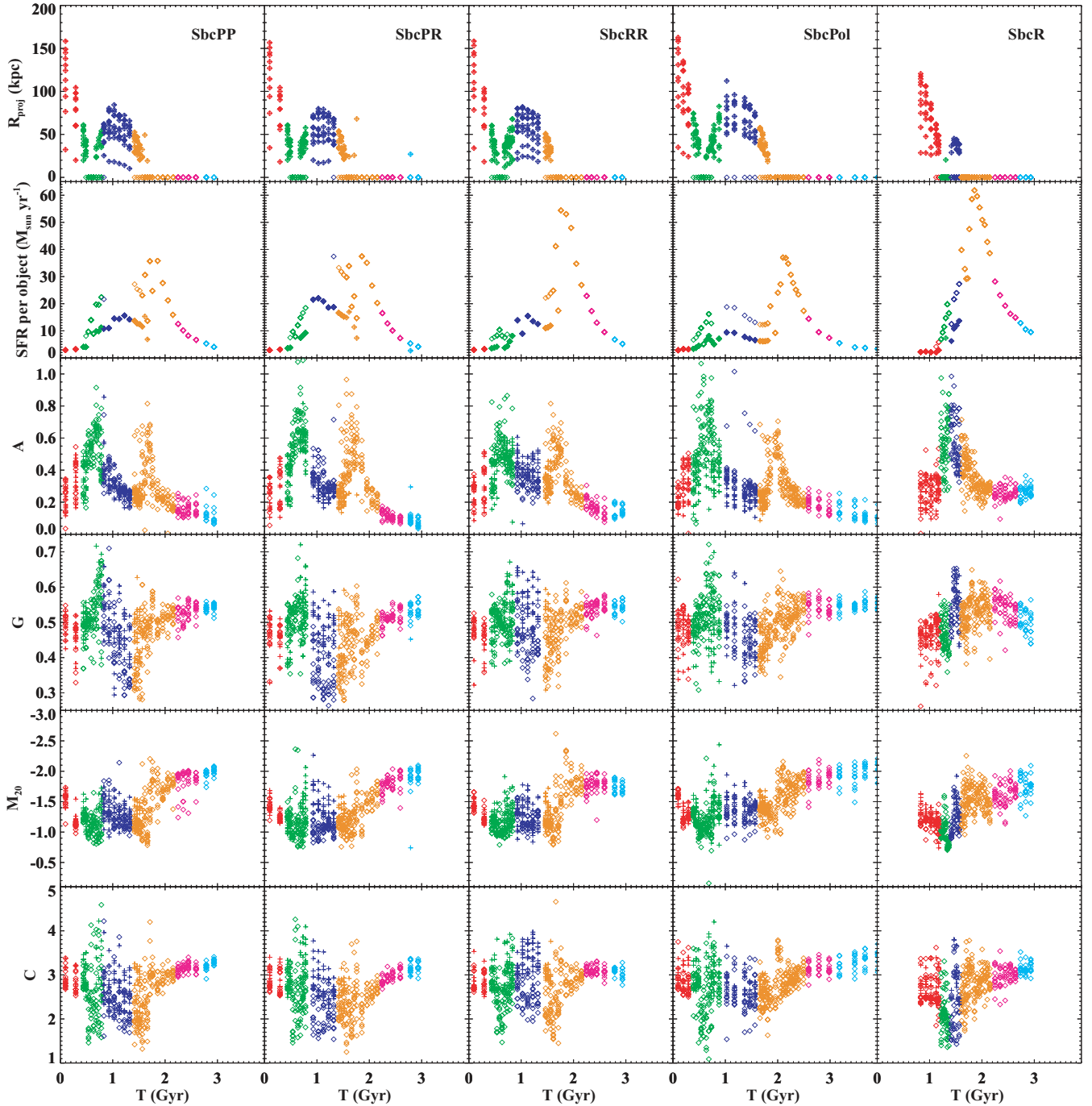
retrograde–retrograde (SbcRR) and polar (SbcPol) orientations. All of these simulations have similar orbital decay times, with the polar orientation merger taking a few $\times$ 100 Myr longer for the final merger to occur (Table 3). All of the parabolic Sbc simulations experience peaks in star formation and asymmetry at the first pass and the final merger, with the maximum star formation rate depending on the relative orientation of the discs (Fig. 11). The strength of the morphological disturbances also depends on the orientation of the galaxies, with the intrinsically asymmetric polar and retrograde–prograde mergers showing the highest asymmetries (Fig. 11). The viewing-angle averaged time-scales during which a particular set of quantitative morphologies are disturbed vary by a factor of 2 for these different orientations [$T(G - M_{20}) \sim$0.3–0.6 Gyr, $T(G - A) \sim$0.8–1.3 Gyr and $T(A) \sim$0.7–1.5 Gyr; Table 6, Fig. 12]. This is in reasonable agreement with the $\sim$0.7–1.0 Gyr asymmetry time-scales of the star particles of equal-mass prograde-inclined, retrograde-inclined and prograde–retrograde merger simulations found by Conselice (2006). The retrograde–retrograde merger is disturbed for the longest time for all of the quantitative morphology measures. The time-scales are also sensitive to the criteria used to identify the merger (Table 6; Fig. 12). The typical $T(G - M_{20})$ is $\sim$0.4 Gyr, while $T(A) \sim$ 1.1 Gyr and $T(G - A) \sim$ 1.0 Gyr. The close pair time-scales do not vary strongly with orientation ($\delta T \sim$ 200 Myr; Table 7) but do depend on the range of R_{proj} chosen, with $R_{proj} < 30$ kpc time-scales often significantly shorter than typical $T(G - A)$ and $T(A)$ values. All of the simulations show enhanced star formation for significantly longer periods than the morphological disturbances, with the peaks in the star formation rates often occurring after the peaks in the asymmetry. The remnant morphologies are generally similar (Table 8), although the retrograde–retrograde merger remnant has a higher M_{20} value than the prograde–prograde merger (-1.77 versus -1.93) and both the retrograde–retrograde and polar merger remnants have higher asymmetries (0.15 versus 0.0). The remnant morphologies are more consistent with early-type disc galaxies (Sb) than spheroids (E/S0) (Fig. 13). The remnants are forming stars at $\sim$5–6 $M_\odot$ yr^{-1}.

A subparabolic Sbc–Sbc merger simulation with a highly radial orbit, zero net angular momentum, prograde–retrograde orientation and stiff feedback was also examined (SbcR). Because the galaxies start with low relative velocities, it takes significantly longer for the first pass to occur (1.3 versus 0.6 Gyr). However, there is significantly less time between the first pass and the final merger (0.3 versus 1.1 Gyr; Table 6). As a result, the morphologies and star formation rates as a function of merger stage are quite different from

Table 5. High-resolution prograde–prograde Sbc merger (SbcPP×10) time-scales versus viewing angle.

Camera	$T(G - M_{20})$ (Gyr)	$T(G - A)$ (Gyr)	$T(A)$ (Gyr)	$T(5 < R_p < 20)$ (Gyr)	$T(10 < R_p < 30)$ (Gyr)	$T(10 < R_p < 50)$ (Gyr)	$T(10 < R_p < 100)$ (Gyr)
0	0.24	0.88	0.98	0.05	0.24	0.93	1.30
1	0.32	0.86	0.86	0.00	0.22	1.05	1.20
2	0.44	1.15	1.15	0.49	0.29	0.46	0.61
3	0.27	0.76	0.98	0.00	0.10	0.68	1.20
4	0.10	0.68	0.71	0.27	0.73	1.03	1.03
5	0.39	0.95	0.86	0.17	0.32	0.88	1.20
6	0.24	1.15	1.05	0.10	0.24	0.93	1.34
7	0.27	0.83	1.10	0.15	0.83	0.93	1.25
8	0.15	0.86	0.81	0.05	0.29	1.08	1.25
9	0.20	0.86	0.86	0.10	0.36	1.10	1.25
10	0.20	0.90	1.00	0.00	0.22	0.88	1.05
Mean	0.26 ± 0.10	0.90 ± 0.14	0.94 ± 0.13	0.15 ± 0.18	0.39 ± 0.22	1.00 ± 0.17	1.22 ± 0.20

Computed for time-steps $t > 0.6$ Gyr, as discussed in Section 4.1. The camera angles are given in Section 2.2.

© 2008 The Authors. Journal compilation © 2008 RAS, MNRAS **391**, 1137–1162

Figure 11. Time versus R_{proj}, star formation rate per object, A, G, M_{20} and C for the standard resolution prograde–prograde Sbc merger (SbcPP), the prograde–retrograde Sbc merger (SbcPR), the retrograde–retrograde Sbc merger (SbcRR), the polar orientation Sbc merger (SbcPol), and the radial orbit Sbc merger (SbcR). Each merger stage is colour-coded as in Fig. 4. The parabolic orbit Sbc mergers show similar peaks in star formation and morphological disturbances at the first pass and final merger, while the radial orbit Sbc merger (SbcR) has a single peak in both star formation and disturbed morphology after the initial encounter.

the parabolic orbit simulations (Figs 11 and 12). Asymmetry peaks during the first pass and maximal separation stages, but is quite low during the final merger. On the other hand, the star formation rate is strongly enhanced throughout the later merger stages and reaches its peak during the final merger. The $G-M_{20}$, $G-A$ and A time-scales are similar to the parabolic $R_{peri} = 11$ Sbc simulations. The close pair time-scales, however, are naturally ~50 per cent shorter than parabolic orbits. The merger remnant has a large bulge surrounding

by a very blue star-forming ring. It has the highest star formation rate ($13\,M_\odot\,yr^{-1}$) of any of the simulations, and because of the bright blue ring, its morphology is the most asymmetric (0.25) and disc-like in its G, M_{20} and C values.

Two additional prograde–prograde parabolic orbit simulations with smaller and larger pericentric distances ($R_{peri} = 5.5$, 44 versus 11 kpc) were analysed. The small R_{peri} simulation (SbcPPr−) takes 340 Myr less to merge, while the large R_{peri} (SbcPPr+) simulation

Table 6. Equal-mass merger morphological time-scales.

Simulation	$T(G-M_{20})$ (Gyr)	$T(G-A)$ (Gyr)	$T(A)$ (Gyr)
	Sbc–Sbc mergers		
SbcPP×10 (no dust)	0.44 ± 0.15	0.89 ± 0.34	1.12 ± 0.40
SbcPP×10	0.26 ± 0.10	0.90 ± 0.14	0.94 ± 0.13
SbcPP×4	0.30 ± 0.11	0.78 ± 0.17	0.80 ± 0.15
SbcPP	0.39 ± 0.16	0.78 ± 0.21	0.74 ± 0.17
SbcPR	0.31 ± 0.10	0.98 ± 0.11	1.12 ± 0.11
SbcRR	0.60 ± 0.18	1.33 ± 0.32	1.46 ± 0.31
SbcPol	0.40 ± 0.25	1.10 ± 0.24	1.10 ± 0.29
SbcPPr−	0.57 ± 0.20	0.77 ± 0.19	0.70 ± 0.16
SbcPPr+	1.03 ± 0.74	0.93 ± 0.48	1.19 ± 0.57
SbcR	0.44 ± 0.21	0.93 ± 0.30	0.61 ± 0.12
SbcPPn = 0	0.42 ± 0.20	0.90 ± 0.35	0.76 ± 0.17
SbcRn = 0	0.23 ± 0.09	0.86 ± 0.35	0.42 ± 0.09
	G–G mergers		
G3PP	0.17 ± 0.06	0.32 ± 0.07	0.22 ± 0.11
G2PP	0.22 ± 0.14	0.31 ± 0.15	0.25 ± 0.19
G1PP	0.24 ± 0.05	0.35 ± 0.14	0.30 ± 0.16
G0PP	0.30 ± 0.09	0.43 ± 0.17	0.39 ± 0.16
G3PPn = 0	0.19 ± 0.08	0.38 ± 0.15	0.19 ± 0.16
G2PPn = 0	0.22 ± 0.06	0.30 ± 0.12	0.21 ± 0.10
G1PPn = 0	0.61 ± 0.24	0.45 ± 0.13	0.30 ± 0.12
G0PPn = 0	0.31 ± 0.09	0.48 ± 0.14	0.41 ± 0.17

Computed for time-steps $t > 0.6\,$Gyr, as discussed in Section 4.1. The standard resolution simulations also have $\delta M_{20} = -0.157$, $\delta A = -0.115$ correction applied, as in the last row of Table 4.

takes an additional 2 Gyr to merge (Table 6, Fig. 14). The merger time-scales and properties of the small R_{peri} simulation are similar to the fiducial SbcPP simulation, with somewhat shorter close pair time-scales for $R_{proj} < 50$ and $100\,h^{-1}$ kpc (Table 7, Fig. 14). The large R_{peri} simulation, however, has little enhanced star formation and lower asymmetries during the first pass, and experiences less enhanced star formation during the final merger because more gas has been consumed in 'normal' disc star formation (Fig. 14). Despite weaker morphological disturbances, the $G - M_{20}$ observability time-scales for the large R_{peri} simulations is significantly larger (1.0 versus 0.4 Gyr) but with larger scatter with viewing angle. The $G - A$ and A time-scales are also longer with larger scatter, as are the close pair time-scales for $R_{proj} < 50$ and 100 kpc. The large R_{peri} remnant has somewhat higher G, M_{20} and C values than the $R_{peri} = 5.5$ and 11 kpc remnants, making its morphology more like typical spheroidals (Table 8). Visual inspection of the remnant shows that the recent star formation in the large R_{peri} is much more centralized, while the smaller R_{peri} simulations have an extended disc of young stars. Because the SbcPPr+ simulation takes twice as long to merge, most of its remnant's cold gas has been consumed in star formation during the merger.

In summary, we find that orientation and large pericentric distances can have a significant effect on the time-scales during which mergers can be identified morphologically. Some relative orientations of the merging system increase the strength of the morphological disturbances (prograde–retrograde, polar), while other orientations increase the time-scales of those disturbances (retrograde–retrograde). Large pericentric distances naturally result in long orbital decay times, which suggest that the duration of the merger is as important to the time-scales of morphological disturbances as the orientation of the merging galaxies. The orbits do affect the timing of the morphological disturbances. Most of

the parabolic orbit simulations show peaks in morphological disturbances at the first pass and final merger. The highly radial orbit simulation shows a single peak in asymmetry during the first pass, while the large pericentric radius simulation shows a less dramatic enhancement of asymmetry during the first pass and final merger. However, the highly radial orbit simulation also has morphological disturbance time-scales that agree with the parabolic orbits to within the scatter associated with the viewing angle. Enhanced star formation rates generally occur for longer durations than the morphological disturbances, with the star formation rates often peaking after the asymmetries. The remnants all have similar concentrations (G, M_{20} and C) consistent with early-type spirals but only the retrograde–retrograde, polar and highly radial orbit merger remnants show significant asymmetries ($A > 0.1$).

4.5 Gas fraction and scalelength

Gas-rich mergers undergo significant starbursts triggered by the varying tidal forces and inflow of gas during the merger. Because these new stars can influence the measured morphologies, it is likely that the amount of gas available to form stars affects morphology time-scales during the merger process. The Sbc galaxy and the G3 galaxy have similar total masses (8.1×10^{11} and $1.2 \times 10^{12}\,M_{\odot}$, respectively), and similar bulge to disc stellar mass ratios (0.25 and 0.21). However, the Sbc galaxy has a much larger gas reservoir with over 50 per cent of its baryons in gas. The G3 galaxy, on the other hand, has only ∼20 per cent of its baryons in gas. Both models assume that the gas disc has a scalelength three times the scalelength of the stellar disc, but the Sbc's gas and stellar discs are twice the adopted scalelengths for the G model. The end result is that the Sbc merger simulations have much more gas at large radii as well as a higher density of gas within the central regions. Cox et al. (2008) found that higher central gas densities lead to less merger-induced star formation when compared to the undisturbed disc star formation. The SbcPP merger has less efficient merger-driven star formation throughout the interaction relative to the G3PP merger (where efficiency refers to the fraction of total gas converted to stars), with the SbcPP and G3PP mergers showing 23 and 46 per cent more star formation than their undisturbed counterparts, respectively. However, the SbcPP merger experiences higher star formation rates in general and at the first pass and final merger in particular, reflecting its high gas fraction.

We compare the time-dependent morphologies and projected separations for prograde–prograde parabolic orbit mergers with stiff feedback for the Sbc and G3 galaxies (SbcPP and G3PP; Figs 11 and 15). We find that the merger time-scales and morphologies are also affected by the gas disc properties. Despite similar pericentric distances, the G3PP simulation takes about 700 Myr longer for the nuclei to coalesce than the SbcPP simulation. As a result, the time-scales during which the merging galaxies can be identified as a close pair are also longer. The G3PP simulation spends three times longer as a very close pair ($R_{proj} < 30\,h^{-1}$ kpc) than the SbcPP simulation (Table 7). However, the time-scales for morphological disturbances are shorter for the lower gas fraction G3PP simulation by a factor of ∼2–4 (Table 6). Although the G3PP merger is more efficient at turning the available gas into stars than the SbcPP merger, the G3PP merger has less star formation overall because of its larger bulge and lower gas fraction (Figs 15 and 17). The G3PP merger experiences less star formation along tidal arms and lower asymmetries at the first pass than the SbcPP merger. Nevertheless, the remnants have similar quantitative morphologies and star formation rates (Table 8). Both simulations produce dusty remnants with
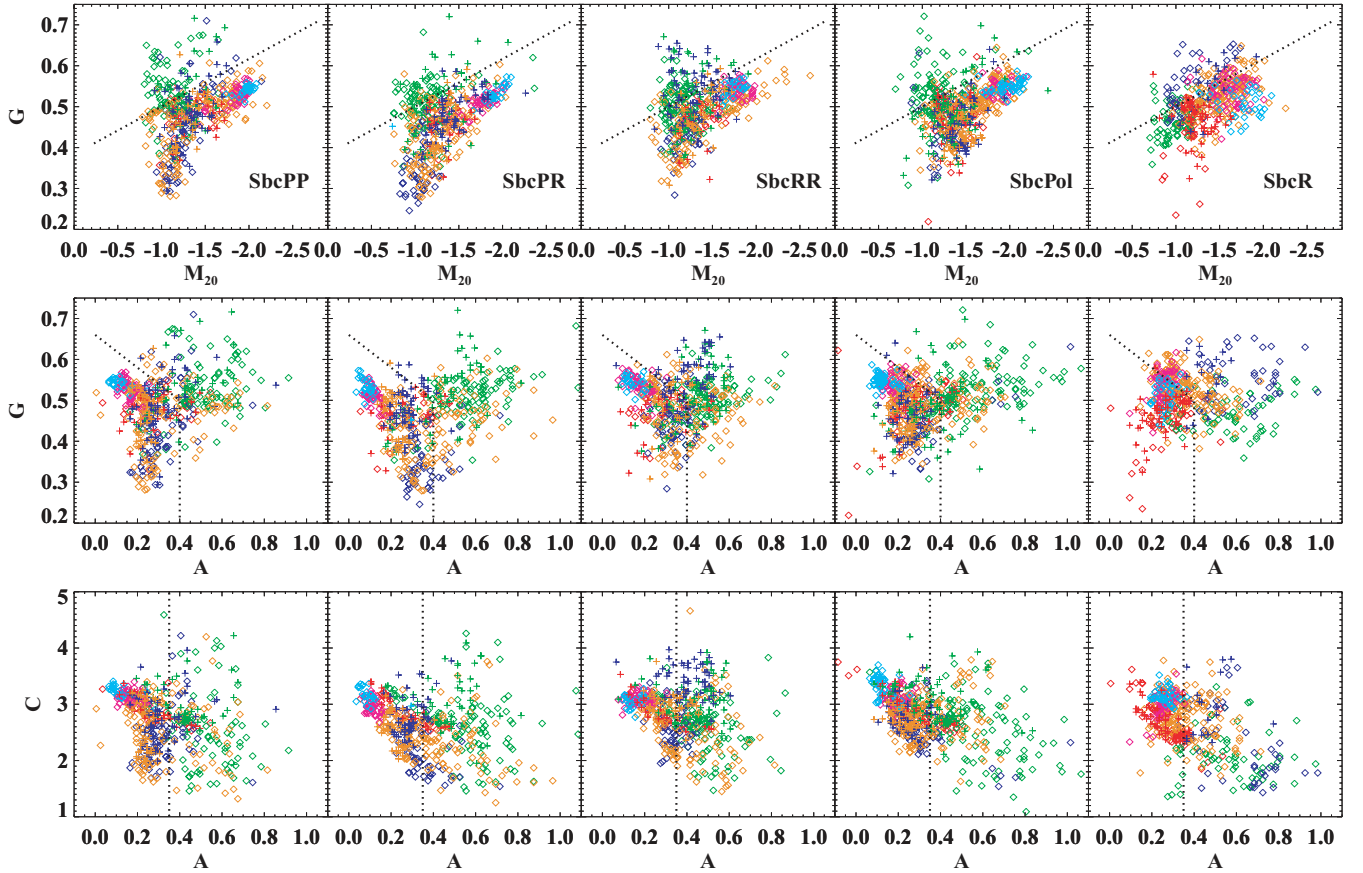
Figure 12. $G - M_{20}$, $G - A$ and $C - A$ for the same simulations as Fig. 11 (SbcPP, SbcPR, SbcRR, SbcPol and SbcR). Each merger stage is colour-coded as in Fig. 4. The SbcRR and SbcR simulations are more likely to have disturbed morphologies during the maximal separation stage between the first pass and final merger (blue points) than the other Sbc simulations.

Table 7. Equal-mass close pair time-scales.

| Simulation	$T(5 < R_{proj} < 20)$ (Gyr)	$T(10 < R_{proj} < 30)$ (Gyr)	$T(10 < R_{proj} < 50)$ (Gyr)	$T(10 < R_{proj} < 100)$ (Gyr)
		Sbc–Sbc mergers		
SbcPP×10	0.15 ± 0.18	0.39 ± 0.22	1.00 ± 0.17	1.22 ± 0.20
SbcPP×4	0.26 ± 0.21	0.53 ± 0.31	1.12 ± 0.17	1.34 ± 0.19
SbcPP	0.15 ± 0.19	0.35 ± 0.23	0.90 ± 0.16	1.20 ± 0.18
SbcPR	0.27 ± 0.49	0.54 ± 0.50	1.08 ± 0.59	1.37 ± 0.55
SbcRR	0.16 ± 0.26	0.44 ± 0.35	0.97 ± 0.24	1.31 ± 0.14
SbcPPr−	0.13 ± 0.10	0.43 ± 0.16	0.78 ± 0.11	0.99 ± 0.15
SbcPPr+	0.26 ± 0.29	0.50 ± 0.43	1.38 ± 0.92	3.06 ± 0.52
SbcPol	0.10 ± 0.08	0.34 ± 0.18	0.92 ± 0.38	1.45 ± 0.26
SbcR	0.08 ± 0.20	0.18 ± 0.18	0.36 ± 0.18	0.84 ± 0.09
SbcPPn = 0	0.15 ± 0.20	0.43 ± 0.28	0.96 ± 0.17	1.27 ± 0.15
SbcRn = 0	0.03 ± 0.06	0.13 ± 0.19	0.29 ± 0.21	0.77 ± 0.05
		G–G mergers		
G3PP	0.39 ± 0.30	0.72 ± 0.39	1.21 ± 0.38	1.85 ± 0.13
G2PP[a]	0.43 ± 0.20	0.60 ± 0.16	0.71 ± 0.20	–
G1PP[b]	0.58 ± 0.13	0.52 ± 0.16	0.64 ± 0.20	–
G0PP[c]	0.67 ± 0.19	0.39 ± 0.22	–	–
G3PPn = 0	0.30 ± 0.38	0.56 ± 0.39	1.10 ± 0.37	1.72 ± 0.13
G2PPn = 0[a]	0.39 ± 0.16	0.62 ± 0.17	0.70 ± 0.20	–
G1PPn = 0[b]	0.54 ± 0.09	0.50 ± 0.17	0.54 ± 0.20	–
G0PPn = 0[c]	0.64 ± 0.17	0.38 ± 0.21	–	–

R_{proj} has units h^{-1} kpc. Time-scales for simulations with starting separations less than maximum R_{proj} are not calculated.
[a]Initial separation is $70\,h^{-1}$ kpc. [b]Initial separation is $56\,h^{-1}$ kpc. [c]Initial separation is $42\,h^{-1}$ kpc.

Table 8. Equal-mass merger remnant properties.

Simulation	G	M_{20}	C	A	SFR ($M_\odot$ yr^{-1})
		Sbc–Sbc mergers			
SbcPP×10 (no dust)	0.59 ± 0.03	-1.75 ± 0.39	4.1 ± 0.3	0.05 ± 0.02	5.82
SbcPP×10	0.54 ± 0.01	-1.80 ± 0.23	3.4 ± 0.3	0.15 ± 0.07	5.82
SbcPP×4	0.55 ± 0.01	-1.98 ± 0.07	3.6 ± 0.1	0.16 ± 0.05	5.28
SbcPP	0.54 ± 0.01	-1.93 ± 0.09	3.2 ± 0.1	0.00 ± 0.48	5.24
SbcPR	0.53 ± 0.02	-1.91 ± 0.11	3.2 ± 0.1	0.09 ± 0.02	5.11
SbcRR	0.54 ± 0.02	-1.77 ± 0.11	3.1 ± 0.1	0.14 ± 0.04	6.78
SbcPPr−	0.53 ± 0.03	-1.85 ± 0.20	3.1 ± 0.2	0.08 ± 0.10	4.58
SbcPPr+	0.59 ± 0.04	-1.94 ± 0.28	3.5 ± 0.2	0.01 ± 0.10	3.68
SbcPol	0.55 ± 0.02	-1.92 ± 0.14	3.2 ± 0.2	0.16 ± 0.05	5.45
SbcR	0.52 ± 0.03	-1.80 ± 0.22	3.2 ± 0.2	0.25 ± 0.04	12.85
SbcPPn = 0	0.59 ± 0.04	-2.46 ± 0.38	4.5 ± 0.6	0.12 ± 0.08	3.41
SbcRn = 0	0.54 ± 0.04	-2.21 ± 0.49	3.9 ± 0.9	0.22 ± 0.04	8.33
		G–G mergers			
G3PP	0.55 ± 0.05	-1.93 ± 0.10	3.2 ± 0.3	0.03 ± 0.02	3.11
G2PP	0.56 ± 0.02	-1.83 ± 0.14	3.2 ± 0.2	0.01 ± 0.04	1.97
G1PP	0.53 ± 0.01	-1.92 ± 0.05	3.2 ± 0.2	-0.02 ± 0.03	0.68
G0PP	0.50 ± 0.01	-1.73 ± 0.06	3.2 ± 0.8	0.03 ± 0.04	0.38
G3PPn = 0	0.57 ± 0.02	-2.37 ± 0.20	4.2 ± 0.5	0.04 ± 0.03	1.88
G2PPn = 0	0.57 ± 0.01	-2.25 ± 0.12	4.1 ± 0.4	-0.01 ± 0.03	0.95
G1PPn = 0	0.60 ± 0.01	-2.04 ± 0.07	4.9 ± 0.7	-0.05 ± 0.02	0.13
G0PPn = 0	0.52 ± 0.02	-1.73 ± 0.06	3.8 ± 0.5	-0.01 ± 0.02	0.03

The properties of the simulated merger remnants observed 1 Gyr after the coalescence of the nuclei.
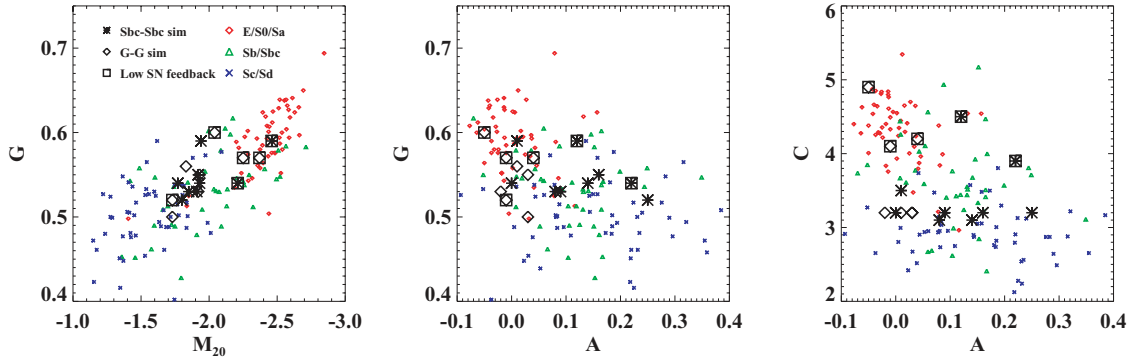
Figure 13. Simulated merger remnant morphologies, including the effects of dust, for $G - M_{20}$, $G - A$ and $C - A$. The Sbc–Sbc remnants are black asterisks, and the G–G remnants are black diamonds. Simulations run with $n = 0$ supernova feedback are surrounded by a black square. Also plotted are the SDSS g or B morphologies of local galaxies from SDSS and the Frei et al. catalogue, measured by LPM04. The remnants of all the simulations run with stiff $n = 2$ supernova feedback have quantitative morphologies similar to Sb galaxies (green triangles). Some simulations with isothermal $n = 0$ supernova feedback approach E/S0 morphologies (red diamonds).

G, M_{20}, C and A values consistent with bulge-dominated spirals (Fig. 13). Both remnants have significant residual star formation (3–5 $M_\odot$ yr^{-1}) and dust reddening.

4.6 Mass

The total mass involved in the merger may also affect morphologies and star formation rates, as larger galaxies have deeper potential wells and produce stronger tidal forces. Equal-mass prograde–prograde merger simulations spanning a factor of 23 in total mass and a factor of 50 in stellar mass were examined to explore the effects of merger mass (G3PP, G2PP, G1PP and G0PP simulations). The progenitor galaxies have increasing gas fractions and total mass to light ratios with decreasing mass (Table 1). Both supernova feedback models were explored for all the G-series mergers. The orbits
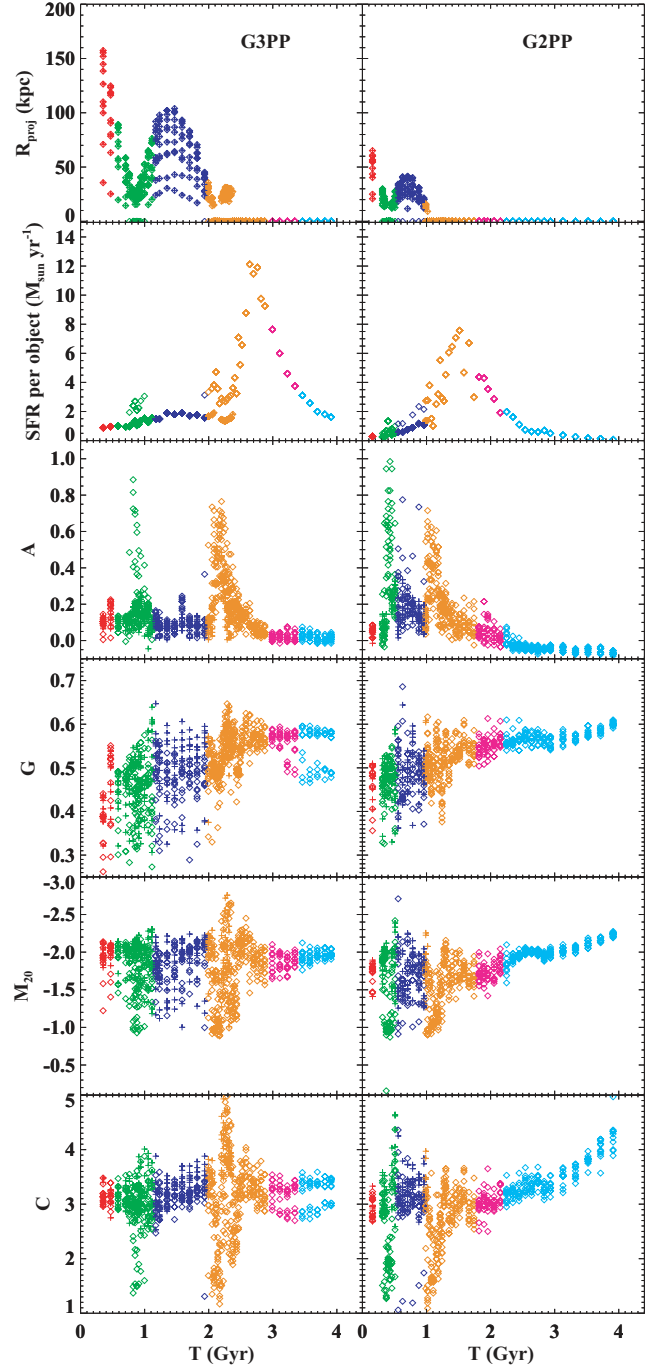
for all of the G-series mergers are slightly subparabolic, with eccentricities $e = 0.95$. This significantly shortens the decay times for the G1 and G0 mergers, and hence may result in shorter close pair time-scales than would be observed for $e = 1.0$ orbits. We do not expect this to impact the morphology observability time-scales, as disturbed morphologies are apparent only at the first pass and final merger stages. The initial separations are less than $100\,h^{-1}$ kpc for the G2, G1 and G0 mergers, and so close pair time-scales are not computed when the initial separation is less than the measured range of projected separations (Table 7).

We find that all of the equal-mass G-series mergers show similar correlations of the morphologies with merger stage. The morphological disturbance time-scales are ∼100–200 Myr longer for the lowest mass merger (G0PP) than the highest mass merger (G3PP; Table 6, Figs 15 and 16). However, the time between the first pass
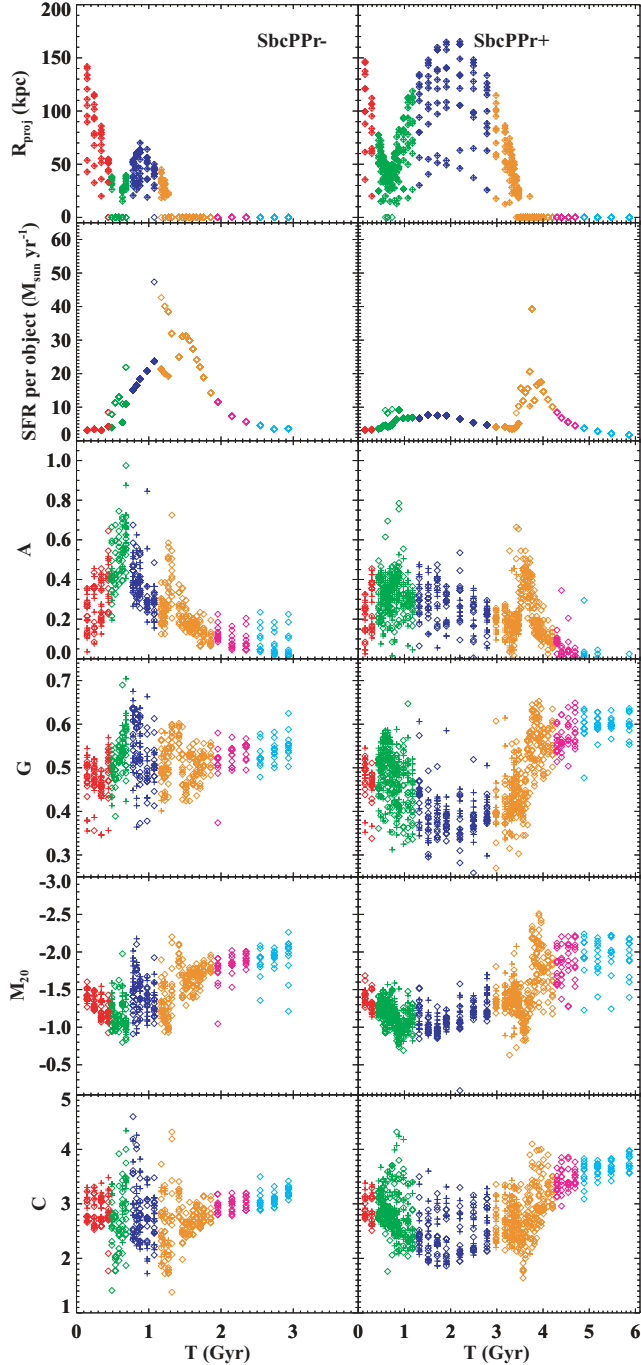
Figure 14. Time versus R_{proj}, star formation rate per object, A, G, M_{20} and C for the standard resolution prograde–prograde Sbc mergers with small R_{peri} (SbcPPr−) and large R_{peri} (SbcPPr+). Each merger stage is colour-coded as in Fig. 4. The large R_{peri} simulation takes significantly longer to merge, and has lower peak star formation rates and asymmetries.

Figure 15. Time versus R_{proj}, star formation rate per object, A, G, M_{20} and C for the prograde–prograde 1.2×10^{12} M$_\odot$ G3 merger (G3PP) and less massive prograde–prograde 5×10^{11} M$_\odot$ G2 merger (G2PP). Each merger stage is colour-coded as in Fig. 4. The G3 merger is less morphologically disturbed than the Sbc prograde–prograde merger (SbcPP) during the first pass, and experiences a peak in the star formation rate well after the peak in asymmetry at the final merger.

and coalescence of the nuclei is ∼ a factor of 2 less for the lower mass merger than the highest mass merger (Table 6, Fig. 17), and the close pair time-scales at $10 < R_{proj} < 30\,h^{-1}$ kpc reflect this (Table 7). The close pair time-scales at $5 < R_{proj} < 20\,h^{-1}$ kpc show longer time-scales for the lowest mass merger. This is an artefact of the object detection algorithm. Larger galaxies are most likely to be counted as one object at small separations because they have larger scalelengths and overlapping isophotes. The merger remnants

for all but the lowest mass merger (G0PP) are remarkably similar in their morphology, with the lower mass remnants showing lower star formation rates and extinctions. The G0PP remnants are more disc-like in their G and M_{20} values, even when $n = 0$ feedback is adopted.

4.7 Supernova feedback

The parabolic prograde–prograde and radial prograde–retrograde Sbc simulations and all of the G-series simulations were run with both supernova feedback models. Although the total gas consumption and star formation during the merger are similar for both feedback scenarios (Cox et al. 2006, 2008), the isothermal $n = 0$ feedback simulations with parabolic orbits experience more star formation during the first pass and have less gas available for a second starburst during the final merger (Cox et al. 2006). The opposite is true for the highly radial orbit Sbc simulations because there is not enough time between the first pass and final merger for the low feedback simulation to consume large amounts of gas. The $n = 0$ radial orbit Sbc merger experience the highest peak star formation rate of all the merger simulations during the final merger ($> 500 \, M_\odot \, yr^{-1}$), while the $n = 2$ radial orbit Sbc merger experiences its peak star formation rate during the first pass ($\sim 80 \, M_\odot \, yr^{-1}$).

We find that close pair time-scales and morphological disturbances as a function of merger stage and merger time-scales are generally similar for the different feedback models, given the scatter with viewing angle (Tables 6 and 7). The primary difference between the $n = 2$ stiff feedback and the $n = 0$ isothermal feedback simulations appears in the properties of the remnants (Table 8, Figs 13 and 18). The $n = 0$ feedback remnants are significantly more like E/S0 in the quantitative morphologies (G, M_{20} and C) because they have $\sim$40–50 per cent lower gas metallicities and hence less dust to obscure the nuclei. The lower gas metallicities are probably an artefact of our chemical enrichment scheme, rather than a robust prediction of the dust evolution. Supernovae are assumed to produce only metals which enrich surrounding gas particles, but do not produce any gas particles themselves. If all surrounding gas particles are consumed in star formation, the metals which would have be produced in supernova have no place to go and remain locked up in the stars. The $n = 0$ feedback models experience more intense star formation and consume a great amount of their existing gas during the first pass, hence are more effected by these limitations in our model. Nevertheless, while it is unclear if the dust properties of the merger remnants will be strongly affected by feedback, it is likely that the $n = 2$ feedback remnants have too much dust, as we do not include any dust destruction mechanisms.

5 DISCUSSION

Every equal-mass gas-rich merger simulation presented here exhibits quantitatively disturbed morphologies at some point along the merger process. However, it is clear that quantitative morphological classifications based on G, M_{20} and A are sensitive only during the first pass and final merger stages for gas-rich equal-mass mergers, and will miss many interacting galaxies observed between the first pass and final merger as well as many recently merged systems. This is in qualitative agreement with the G, M_{20} and A values and merger stages of local ULIRGs. Two-thirds of the $z \sim 0.1$ ULIRG sample used to calibrate the $G - M_{20}$, $G - A$ and $C - A$ diagrams in LPM04 exhibit double or multiple nuclei, and therefore are merging systems observed at final merger stage before the coalescence of their nuclei or immediately at the first pass when the galaxies appear overlapping in projection (Fig. 3). The $G - M_{20}$, $G - A$ and $C - A$ merger classification cuts used in LPM04 and this paper identify 93, 80 and 76 per cent of the double and multiple nuclei ULIRGs, respectively. The detection efficiency is significantly lower for the single nucleus ULIRGs (46, 71 and
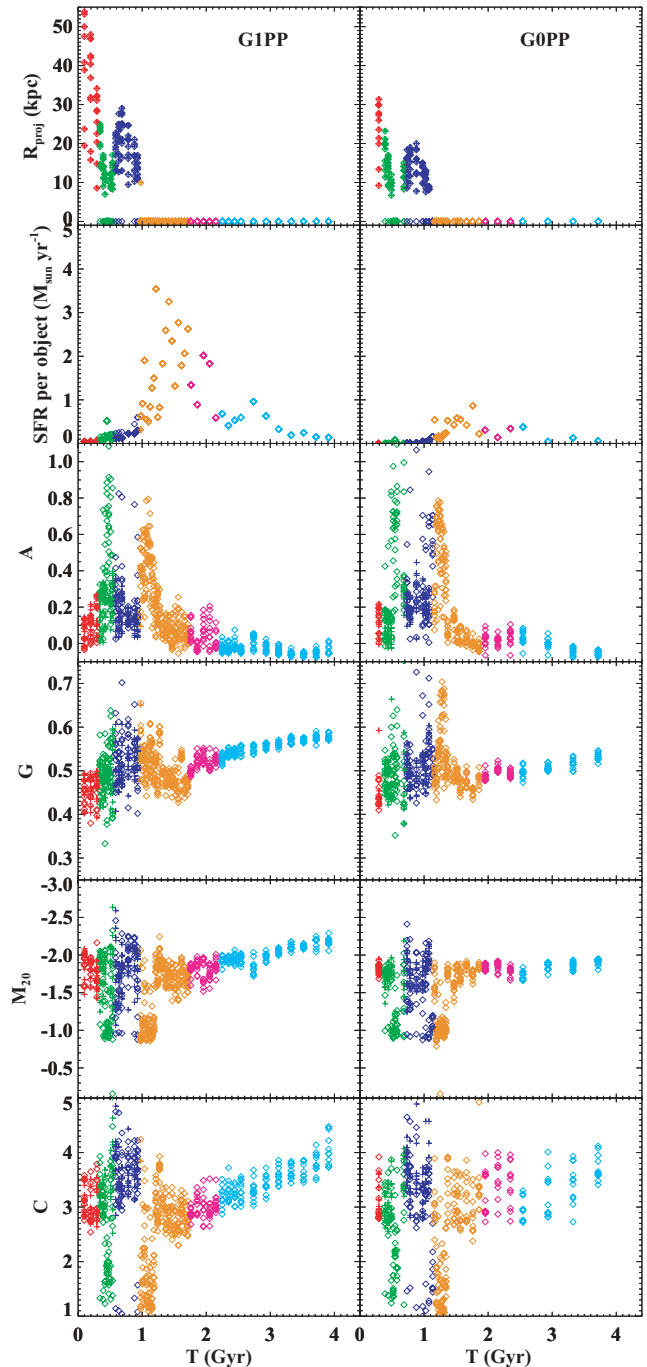

Figure 16. Time versus R_{proj}, star formation rate per object, A, G, M_{20} and C for the prograde–prograde low-mass $2 \times 10^{11} \, M_\odot$ G1 and $5 \times 10^{10} \, M_\odot$ G0 mergers (G1PP, G0PP). Each merger stage is colour-coded as in Fig. 4. The lower mass mergers undergo less star formation but have time-scales for disturbed morphology similar to the more massive G3 and G2 mergers.

54 per cent for $G - M_{20}$, $G - A$ and $C - A$, respectively). This is also in reasonable agreement with our results here, assuming that single nucleus ULIRGs are observed after the first pass or after the coalescence of the nuclei.

The duration, strength and timing of the observed morphological disturbances depend on the merger orientation and orbital parameters, the gas properties of the initial galaxies, and the presence of dust. When dust is included, the merger observability time-scales
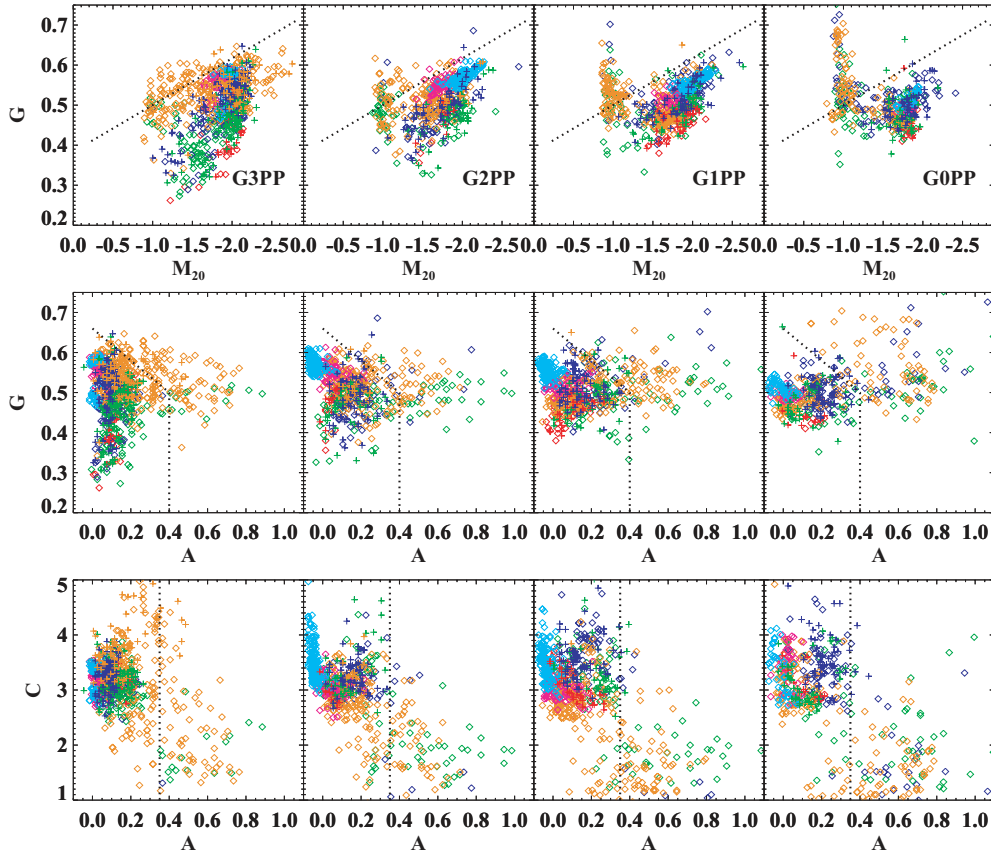
Figure 17. $G - M_{20}$, $G - A$ and $C - A$ for the prograde–prograde G3PP, G2PP, G1PP and G0PP simulations. The simulations span a factor of 23 in total mass, where the virial mass of the initial galaxy is $1.2 \times 10^{12}\,\mathrm{M}_\odot$ for G3, $5.1 \times 10^{11}\,\mathrm{M}_\odot$ for G2, $2.0 \times 10^{11}\,\mathrm{M}_\odot$ for G1 and 5.1×10^{11} for G0. Each merger stage is colour-coded as in Fig. 4. Unlike the Sbc mergers, the G-series simulations are only detected at the final merger (orange points).

depend most strongly on the gas properties, pericentric distance and relative orientation. Galaxies with high gas fractions have more star formation along tidal arms, producing stronger asymmetries during the first pass. Mergers with large impact parameters have long orbital decay time-scales, and exhibit disturbed morphologies for longer. Retrograde–retrograde mergers also show disturbed morphologies for 50–100 per cent longer than prograde–prograde and prograde–retrograde mergers. We find that the supernova feedback prescription and the total mass of the merging galaxies do not have a strong effect on the overall duration of morphological disturbances. The relative orientations affect the strength of the morphological disturbances, with the prograde–retrograde and polar orientations showing the strongest disturbances. The orbital parameters and gas fractions have the strongest influence on the timing of the morphological disturbances. Most of the high gas fraction (Sbc) parabolic orbits show morphological disturbances at the first pass and final merger, while the high gas fraction highly radial orbit and large pericentric distance simulations have weak disturbances at the first pass and stronger disruptions at the final merger. The lower gas fraction (G-series) parabolic orbit simulations experience less star formation and morphological disturbances during the first pass, and hence are most likely to be detected morphologically during the final merger.

Obscuration from dust has a very strong impact on the measured morphologies throughout the merger process until at least 1 Gyr after the coalescence of the nuclei. Dust extinction is highest for the central nuclei where the star formation rates are highest. Because much of the central light is masked by dust, this results in lower G, C and higher M_{20} values during and after the merger. Dust lanes in the remnants can also produce higher asymmetries. However, the inclusion of dust does not significantly change the morphological disturbance time-scales during the prograde–prograde Sbc merger. Our models may overestimate the dust content in the remnants as dust is not destroyed by shock-heating nor is gas removed in a post-merger 'blowout' by an AGN as predicted by other galaxy merger models (e.g. Hopkins et al. 2006). However, dust destruction is expected to be most important after the final merger, when the star formation rate and dust production have sufficiently declined. Therefore, while the dust and gas content of our merger remnants may be overestimated, the morphologies and time-scales calculated during the merger are unlikely to be affected by the destruction/removal of dust at late stages.

The observability time-scales clearly depend on the method used to select merger candidates. The time-scale during which a merging system is a close pair at a particular projected separation is not the same as the time-scale during which the system shows high asymmetries or high $G - M_{20}$ values. The gas-rich Sbc mergers have two to four times longer $T(G - A)$ and $T(A)$ than $T(G - M_{20})$ and $T(10 < R_{\mathrm{proj}} < 30\,h^{-1}\,\mathrm{kpc})$. The lower gas fraction G-series simulations, on the other hand, have similar time-scales for $G - M_{20}$, $G - A$ and A disturbances. Although G and M_{20} are the most affected by dust, the $G - M_{20}$ time-scale is the least affected by the merger parameters with typical time-scales ∼0.2–0.3 Gyr for the G-series simulations and ∼0.3–0.6 Gyr for the Sbc simulations.
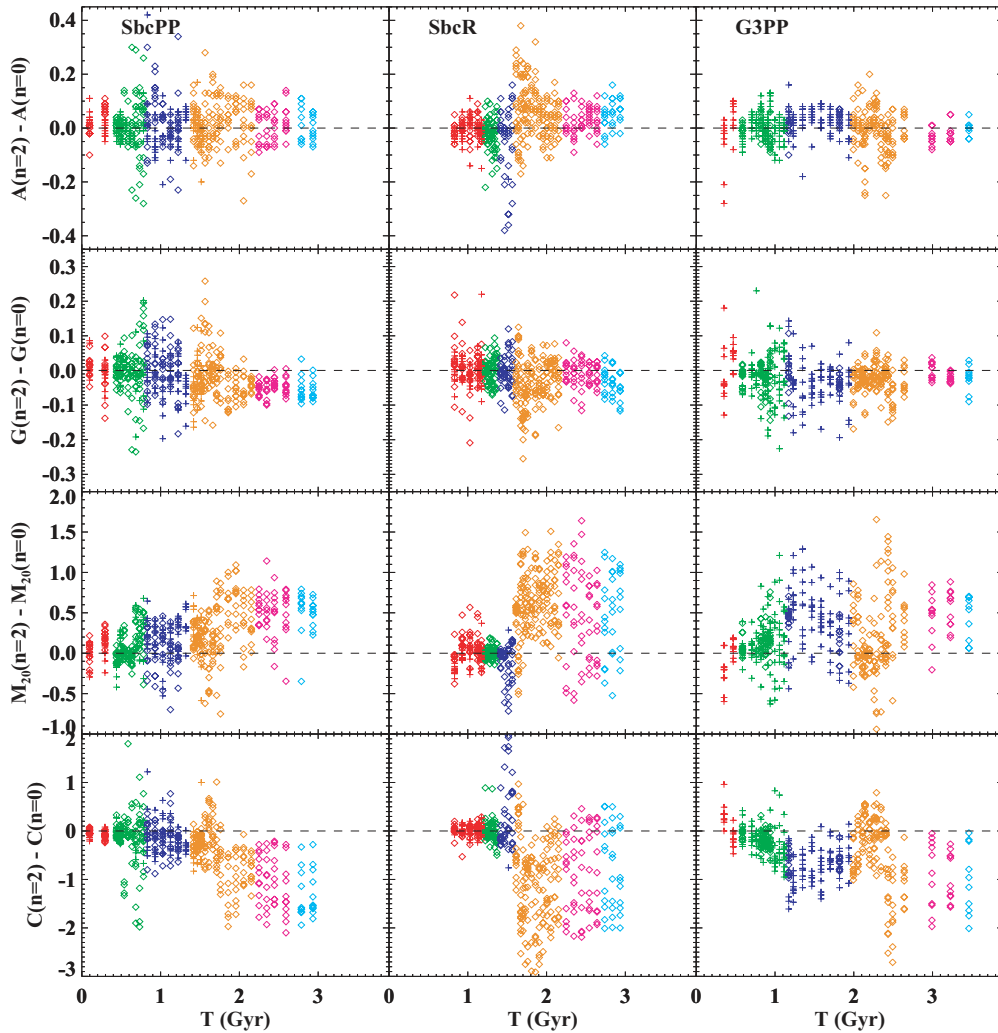
Figure 18. Δ morphology versus time for the simulations with different supernovae feedback prescriptions (SbcPP = prograde–prograde Sbc; SbcR = radial orbit Sbc; G3PP = prograde–prograde G3). The M_{20} values are higher and the concentrations are lower for $n = 2$ 'stiff' supernovae feedback simulations during and after the final merger stage (orange, magenta and cyan points). Each merger stage is colour-coded as in Fig. 4.

The typical $G - A$ time-scales are ∼0.3–0.4 Gyr for the G-series simulations and ∼0.8–1.1 Gyr for the Sbc simulations. The typical A time-scales are ∼0.2–0.3 Gyr for the G-series simulations and ∼0.7–1.1 Gyr for the Sbc simulations. Thus the $G - M_{20}$ time-scales have ∼0.4 Gyr dispersion, while the $G - A$ and A time-scales have ∼0.8 Gyr dispersion. While more mergers may be identified using asymmetry given the longer asymmetry time-scales, the merger rate calculated using $G - M_{20}$ mergers will be less uncertain given the better consistency of the $G - M_{20}$ time-scales.

The close pair time-scales depend on the orbital decay times, with the smaller projected separations showing the greatest fractional variability. For $5 < R_{proj} < 20\,h^{-1}$ kpc, the observability time-scales are ∼0.4–0.6 Gyr for the G-series simulations and ∼0.1–0.3 Gyr for Sbc. These are slightly longer at $10 < R_{proj} < 30\,h^{-1}$ kpc, with time-scales ∼0.5–0.7 Gyr for the G-series simulations and ∼0.2–0.5 Gyr for Sbc. At larger projected radii $<50, 100\,h^{-1}$ kpc, the highly radial orbit and the large pericentric distance parabolic orbit have significantly shorter (∼0.3, 0.8 Gyr) and longer time-scales (∼1.4, 3.0 Gyr), respectively. The typical $10 < R_{proj} < 50\,h^{-1}$ kpc time-scales are ∼0.7–1.2 Gyr for the G3/G2 simulations and ∼0.9–1.1 Gyr for the Sbc simulations. The

typical $10 < R_{proj} < 100\,h^{-1}$ kpc time-scales are ∼1.9 Gyr for the G3 simulations and ∼1.1–1.4 Gyr for the Sbc simulations. Therefore the observability time-scales for close pairs vary by a factor of 4–6 at small projected separations and by a factor of 2–3 at larger separations. It is important to keep in mind that these are the observability time-scales for truly merging pairs (T_{pair} in equation 16) and does not include the contamination correction for non-merging pairs observed in projection [p(merg) in equation 16]. Close pairs with large projected separations are more likely to be contaminated by non-merging galaxies, so the optimal separation distance is likely to be at intermediate separations between 30–$50\,h^{-1}$ kpc.

Unlike our simulated mergers where we know the merger parameters and initial galaxy properties a priori, it is generally impossible to recover these for each galaxy merger observed in large surveys of the distant universe. Ideally, one would like to determine an effective observability time-scale for each method of identifying mergers in order to convert the number density of observed mergers observed into a galaxy merger rate. This effective time-scale should be weighted by the distribution of initial galaxy properties, mass ratios and orbital parameters predicted for galaxy mergers by cosmological simulations. Our work here is a first step towards
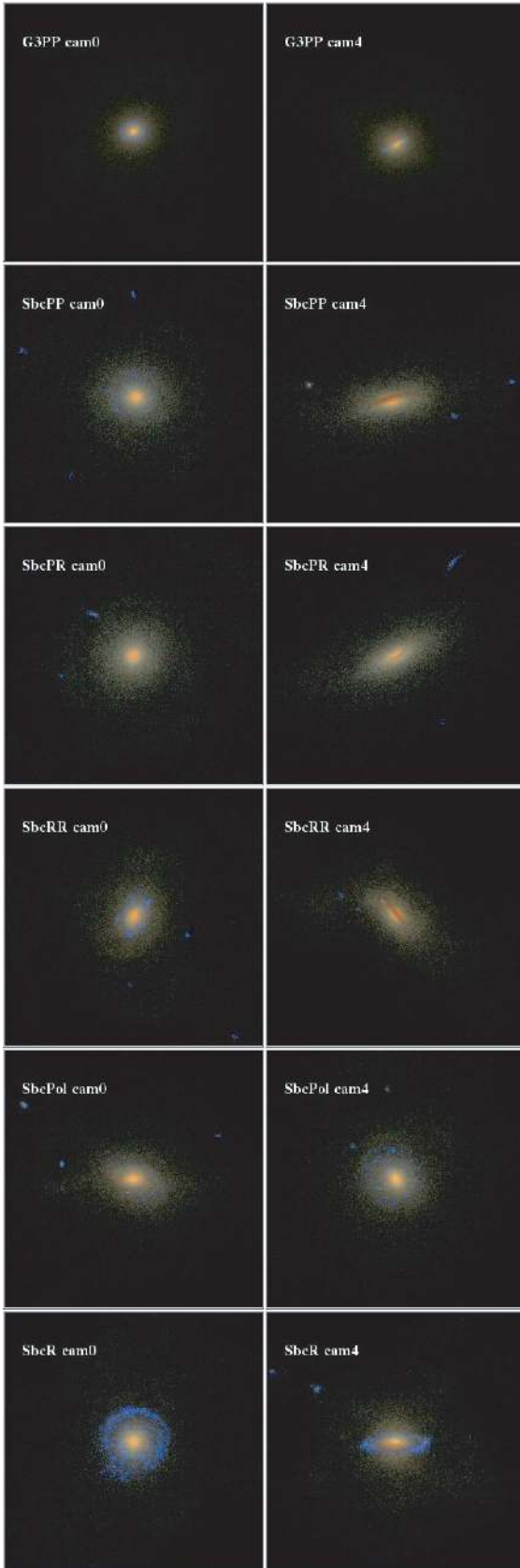
Figure 19. Left-hand panels: G3 and Sbc remnants viewed from camera 0. Right-hand panels: G3 and Sbc remnant viewed from camera 4. All of the remnants show a low-mass dusty star-forming disc as well as a large bulge component.

determining the mean observability time-scale and has concentrated on the systems most likely to be affected by dusty starbursts, i.e. gas-rich equal-mass mergers of discs with small bulges. While this is significant improvement over previous estimates of the morphological disturbance time-scales, it is not sufficient to convert the observed fraction of morphologically disturbed and paired galaxies into a galaxy merger rate. Our next paper will explore the merger observability time-scales of unequal-mass mergers needed to estimate the effective observability time-scale for a realistic population of mergers and calculate the galaxy merger rate.

Galaxy mergers are often assumed to be associated with vigorous starbursts, such as observed for local ULIRGs (e.g. Sanders & Mirabel 1996). Our results here suggest that the timing of morphological disturbances can be offset from the peak in star formation rate, especially if the stiff $n = 2$ supernova feedback prescription is correct. In general, the maximum morphological disturbances occur before the peaks in the star formation rate. While asymmetries experience a sharp peak at the first pass lasting 100–200 Myr, the star formation rate of the system remains enhanced above the initial rate for significantly longer after the first pass for both supernova feedback models. Asymmetries also peak sharply at the final merger, while the star formation peaks after the galaxies appear as single object when the nuclei coalesce. Therefore, the objects with highest star formation rates may not always have the highest asymmetries. This is particularly true for the stiff $n = 2$ supernova feedback models, which experience a long burst at the final merger (∼500 Myr) lasting longer than the high asymmetries (∼200 Myr). During both first pass and final merger, the majority of the enhanced star formation occurs in the nucleus which makes the quantitative morphologies appear more concentrated but not necessarily disturbed. If we ignore the effect of dust on the morphologies, G correlates directly with the star formation rate. Because dust lowers the measured G value, the dusty Sbc final mergers do not show high $G - M_{20}$, while the less obscured G-series final mergers do (Figs 12 and 17).

Roughly 75 per cent of the strongest starbursts in the local universe, ULIRGs, have quantitatively disturbed morphologies, and two-thirds show multiple nuclei. Therefore the correlation between disturbed morphologies and peak star formation rates appears to be better than what is implied by our models. We note that only one of our simulations (the gas-rich, radial orbit, isothermal feedback simulation SbcR$n = 0$) reaches a star formation rate at the final merger that is comparable to ULIRGs. ULIRGs may have higher gas fractions than our models, and often host active nuclei that could destroy or sweep out dust in the central regions during the final merger, both of which would tighten the correlation between disturbed morphologies and high star formation rates. Finally, the star formation rates of some ULIRGs may be overestimated, as some of the infrared luminosity may be from dust heating by an AGN rather than star formation. Any correlation between high star formation rates and disturbed morphologies will depend on the star formation indicator used to calculate the star formation rate. Observed Hα luminosities and equivalent widths are expected to be highest during the first pass and initial starbursts before the star-forming regions have been enshrouded in dust, while infrared luminosities will peak during the final merger after sufficient amounts of metals and dust have been produced (Jonsson et al. 2006).

The vast majority of our equal-mass gas-rich merger remnants are decidedly disc-like and dusty, even those mergers which started with relatively low gas fractions. Previous studies of these and other equal-mass merger simulations have shown that the mass distribution of star particles follow $r^{1/4}$ laws with steep central cusps consistent with or more concentrated than the light profiles of

elliptical galaxies (e.g. Bournaud, Jog & Combes 2005; Cox et al. 2006; Naab, Jesseit & Burkert 2006a; Cox et al. 2008) and lie on the Fundamental Plane (Robertson et al. 2006b). Only simulations with gas fractions >50 per cent (Springel & Hernquist 2005; Robertson et al. 2006a) or mass ratios less than 1:3 (Bournaud et al. 2005; Naab et al. 2006b) have been found to have merger remnants with massive disc components. The masses of our merger remnants are dominated by the bulge component; our merger remnants appear disc-like and less concentrated than elliptical galaxies because we examine the *g*-band light profiles which are strongly affected by both dust extinction in the central regions and a bright but low-mass disc of young stars. Only models with less dusty remnants (as produced by $n = 0$ supernova feedback) or models that ignore dust in the remnant produce remnants with high enough *G*, *C* and low enough M_{20} values to be called spheroids. However, even these spheroidal remnants are forming stars at rates $>1 \, M_{\odot} \, yr^{-1}$, and would not be classified as red E/S0 or post-starburst E + A galaxies. If these simulations accurately represent the end stages of the merger process, a number of 'green' Sb galaxies may be merger remnants (e.g. Hammer et al. 2005). However, our models may overestimate the extinction and star formation during the post-merger stages. Destroying dust by shock-heating would not be sufficient to produce true red and dead spheroids, and additional physics such as feedback from an AGN may be needed to clear out the gas and kill star formation (see also Khalatyan et al. 2008). The remnants forming the fewest stars and with the least dust are those produced by the lowest mass systems. But the low-mass remnants are the least centrally concentrated of all the simulated remnants. Like their higher mass counterparts, the low-mass remnants have more gas ($\sim 10^8 \, M_{\odot}$) and star formation than typical dwarf ellipticals.

6 SUMMARY

We present a morphological analysis of a large suite of GADGET *N*-body/SPH equal-mass gas-rich disc galaxy merger simulations which have been processed through the Monte Carlo radiative transfer code SUNRISE. With the resulting images, we have examined the dependence of quantitative morphology and projected separation in the SDSS *g* band on merger stage, dust, viewing angle, merger orientation and orbital parameters, gas properties, supernova feedback prescription and total mass. We have determined the time-scales for quantitative morphological disturbances in the Gini coefficient, M_{20}, *C* and *A*, and the time-scale during which close pairs lie at projected separations $R_{proj} < 20, 30, 50$ and $100 \, h^{-1}$ kpc. We also examine the merger remnant morphologies and star formation rates.

(i) All of the equal-mass gas-rich merger simulations experience quantitatively disturbed morphologies in $G - M_{20}$, $G - A$ and *A* at the first pass and/or the final merger. This is in good agreement with the morphologies and merger stages of the local ULIRG sample used to empirically calibrate these quantities. However, merging galaxies observed between the first pass and final merger or after the coalescence of their nuclei may not show disturbed $G - M_{20}$ and asymmetries.

(ii) The time-scale during which an equal-mass gas-rich merger may be identified is strongly dependent on the method used to find the merger. The $G - M_{20}$ time-scales are the shortest of the morphological methods, but have the least dependence on the merger parameters with $T(G - M_{20}) \sim 0.2$–0.6 Gyr. The asymmetry time-scales vary by a factor of 3–4 between ~ 0.2–1.1 Gyr, and the $G - A$ time-scales are the longest, with $T(G - A) \sim 0.3$–1.2 Gyr. The close pair time-scales vary by factor of 2–6 with the orbital pa-

rameters, depending on the projected separations adopted. At $5 < R_{proj} < 20 \, h^{-1}$ kpc, the observability time-scales are ~ 0.1–0.6 Gyr. At $10 < R_{proj} < 30 \, h^{-1}$ kpc, the observability time-scales are ~ 0.2–0.7 Gyr. At $10 < R_{proj} < 50 \, h^{-1}$ kpc, the typical observability time-scales are ~ 0.7–1.2 Gyr. At $10 < R_{proj} < 100 \, h^{-1}$ kpc, the typical observability time-scales are ~ 1.1–1.9 Gyr.

(iii) The presence of dust has strong impact on the quantitative morphological measurements, lowering *G* and *C*, raising M_{20} throughout the merger, and raising *A* during the post-merger and remnant stages.

(iv) When dust is included, the time-scales for morphological disturbances are most sensitive to the gas fraction of the merging galaxies, their pericentric distance and relative orientation. The supernova feedback prescription and the total mass of system do not significantly change the morphological time-scales. The relative orientations also affect the strength of the morphological disturbances, with prograde–retrograde and polar orientation showing the highest asymmetries. The timing of the disturbances also depends on orbital parameters and gas fractions, with low gas fractions, large pericentric distances and highly radial orbits showing strong disturbances primarily during the final merger.

(v) The timing of morphological disturbances is generally offset from the peak in star formation rates, with strong morphological disturbances occurring before bursts of merger-induced star formation and for shorter durations. Hence, not all merger-induced starbursts will exhibit morphological disturbances and vice versa. The mode of supernova feedback and dust production also plays important roles in the correlation between morphological disturbances and observed star formation indicators.

(vi) The majority of simulated merger remnants observed ≥1 Gyr after the coalescence of their nuclei appear disc-like and dusty in *g*-band light and are consistent with early-type spiral morphologies and star formation rates. Decreased dust extinction would make most remnants appear more spheroidal, but would not affect the remnants' high star formation rates (typically $>1 \, M_{\odot} \, yr^{-1}$). A major gas-rich merger without AGN feedback does not, by itself, produce a red and dead spheroidal galaxy.

REFERENCES

Abraham R. G., Valdes F., Yee H. K. C., van den Bergh S., 1994, ApJ, 432, 75

Abraham R., van den Bergh S., Nair P., 2003, ApJ, 588, 218

Abraham R. et al., 2007, ApJ, 669, 184

Barton E. J., Geller M. J., Kenyon S. J., 2000, ApJ, 530, 660

Bell E. F., de Jong R. S., 2001, ApJ, 550, 212

Bell E. F., McIntosh D. H., Katz N., Weinberg M. D., 2003, ApJ, 585, L117

Bell E. F. et al., 2004, ApJ, 608, 752

Bell E. F., Phelps S., Somerville R., Wolf C., Borch A., Meisenheimer K., 2006a, ApJ, 652, 270

Bell E. F. et al., 2006b, ApJ, 640, 241

Berrier J. C., Bullock J. S., Barton E. J., Guenther H. D., Zentner A., Wechsler R., 2006, ApJ, 652, 56

Bershady M., Jangren A., Conselice C., 2000, AJ, 119, 2645

Bertin E., Arnouts B., 1996, A&AS, 117, 393

Borne K. D., Bushouse H., Lucas R. A., Colina L., 2000, ApJ, 529, L77

Bournaud F., Jog C. J., Combes F., 2005, A&A, 437, 69

Boylan-Kolchin M., Ma C.-P., Quataert E., 2005, MNRAS, 362, 184

Boylan-Kolchin M., Ma C.-P., Quataert E., 2008, MNRAS, 383, 93

Brinchmann J. et al., 1998, ApJ, 499, 112

Broeils A. H., van Woerden H., 1994, A&AS, 107, 129

Brown M. et al., 2007, ApJ, 654, 858

Bundy K., Ellis R. S., Conselice C., 2005, ApJ, 625, 621

Conselice C., 2003, ApJS, 147, 1

Conselice C., 2006, ApJ, 638, 686

Conselice C., Bershady M. A., Jansen A., 2000, ApJ, 529, 886

Conselice C., Bershady M. A., Dickinson M., Papovich C., 2003, AJ, 126, 1183

Conselice C., Blackburne J., Papovich C., 2005, ApJ, 620, 564

Cox T. J., Primack J. R., Jonsson P., Somerville R. S., 2004, ApJ, 607, L87

Cox T. J., Jonsson P., Primack J. R., Somerville R. S., 2006, MNRAS, 373, 1013

Cox T. J., Jonsson P., Somerville R. S., Primack J. R., Dekel A., 2008, MNRAS, 384, 386

Dasyra K. M. et al., 2006, ApJ, 638, 745

Dekel A., Birnboim Y., 2006, MNRAS, 368, 2

de Jong R. S., 1996, A&A, 313, 45

de Propris R., Liske J., Driver S. P., Allen P., Cross N. J. G., 2005, AJ, 130, 1516

Faber S. M. et al., 2007, ApJ, 665, 265

Fanning D., 2002, Coyote's Guide to IDL Programming (http://www.dfanning.com)

Glasser G. J., 1962, Am. Stat. Assoc., 57, 648

Guo Q., White S., 2008, MNRAS, 384, 2

Hammer F., Flores H., Elbaz D., Zheng X. Z., Liang Y. C., Cesarsky C., 2005, A&A, 430, 115

Hogg D., Masjedi M., Berlind A., Blanton M., Quintero A., Brinkmann J., 2006, ApJ, 650, 763

Hopkins P., Herniquist L., Cox T. J., Di Matteo T., Robertson B., Springel V., 2006, ApJS, 163, 1

Hopkins P., Bundy K., Hernquist L., Ellis R., 2007, ApJ, 659, 976

Iono D., Yun M. S., Mihos J. C., 2004, ApJ, 616, 199

Jiang C. Y., Jing Y. P., Faltenbacher A., Lin W. P., Li C., 2008, ApJ, 675, 1095

Jogee S. et al., 2008, ApJ, submitted

Jonsson P., 2006, MNRAS, 372, 2

Jonsson P., Cox T. J., Primack J., Somerville R., 2006, ApJ, 637, 255

Katz N., Weinberg D. H., Hernquist L., 1996, ApJS, 105, 19

Kampczyk P. et al., 2007, ApJS, 172, 329

Kartaltepe J. S. et al., 2007, ApJS, 172, 320

Kauffmann G., White S. D. M., Guiderdoni B., 1993, MNRAS, 264, 201

Kennicutt R. C., 1998, ApJ, 498, 541

Kereš D., Katz N., Weinberg D. H., Dave R., 2005, MNRAS, 363, 2

Khalatyan A., Cattaneo A., Schramm M., Gottlober S., Steinmetz M., Wisotzki L., 2008, MNRAS, 387, 13

Kitzbichler M., White S., 2008, MNRAS, preprint (arXiv:0804.1965)

Law D. et al., 2007, ApJ, 656, L1

Leitherer C. et al., 1999, ApJS, 123, 3

Li C., Kauffmann G., Heckman T., Jing Y. P., White S. D. M., 2008, MNRAS, 385, 1903

Lin L. et al., 2004, ApJ, 617, L9

Lin L. et al., 2008, ApJ, 681, 232

Lorenz M. O., 1905, Am. Stat. Assoc., 9, 209

Lotz J. M., Primack J., Madau P., 2004, AJ, 613, 262 (LPM04)

Lotz J. M. et al., 2008, ApJ, 672, 177

Masjedi M. et al., 2006, ApJ, 644, 54

Masjedi M., Hogg D. W., Blanton M. R., 2008, ApJ, 679, 260

Mihos J. C., Hernquist L., 1996, ApJ, 464, 641

Moore B., Lake G., Katz N., 1998, ApJ, 495, 139

Naab T., Jesseit R., Burkert A., 2006a, MNRAS, 372, 839

Naab T., Khochfar S., Burkert A., 2006b, ApJ, 636, 81

Patton D., 2000, ApJ, 536, 153

Patton D. et al., 2000, ApJ, 536, 153

Patton D. R. et al., 2002, ApJ, 565, 208

Petrosian V., 1976, ApJ, 209, L1

Ravindranath S. et al., 2006, ApJ, 652, 963

Renzini A., 2007, in Afonso J., Ferguson H. C., Mobasher B., Norris R., eds, ASP Conf. Ser. Vol. 380, At the Edge of the Universe: Latest Results from Deepest Astronomical Surveys. Astron. Soc. Pac., San Francisco, p. 309

Roberts M. S., Haynes M. P., 1994, ARA&A, 32, 115

Robertson B., Bullock J., Cox T. J., di Matteo T., Hernquist L., Springel V., Yoshida N., 2006a, ApJ, 645, 986

Robertson B., Cox T. J., Hernquist L., Franx M., Hopkins P., Martini P., Springel V., 2006b, ApJ, 641, 21

Rocha M., Jonsson P., Primack J. R., Cox T. J., 2008, MNRAS, 383, 1281

Ryan R. E., Cohen S. H., Windhorst R. A., Silk J., 2008, ApJ, 678, 751

Sanders D. B., Mirabel I. F., 1996, ARA&A, 34, 749

Scarlata C. et al., 2007, ApJS, 172, 406

Shen S. et al., 2003, MNRAS, 343, 978

Somerville R. S., Primack J. R., Faber S. M., 2001, MNRAS, 320, 504

Springel V., Hernquist L., 2002, MNRAS, 333, 649

Springel V., Hernquist L., 2003, MNRAS, 339, 289

Springel V., Hernquist L., 2005, ApJ, 622, L9

Springel V., Yoshida N., White S. D. M., 2001, New Astron., 6, 79

Stewart K., Bullock J., Wechsler R., Maller A. H., Zentner A., 2008, ApJ, 683, 597

Takamiya M., 1999, ApJS, 122, 109

Toomre A., 1977, in Tinsely B. M., Larson R., eds, Evolution of Galaxies and Stellar Populations. Yale University Observatory, New Haven, p. 401

This paper has been typeset from a TeX/LaTeX file prepared by the author.